理學博士學位論文

Structural Basis for Differential Transcription Activation by Enantiomeric Agonists of PPARγ and Crystal Structure of TNF-α-Inducing Protein (Tipα) from *Helicobacter pylori*

2016年 8月

서울大學校 大學院

化學部 生化學專攻

장 준 영

Structural Basis for Differential Transcription Activation by Enantiomeric Agonists of PPARγ and Crystal Structure of TNF-α-Inducing Protein (Tipα) from *Helicobacter pylori*

Thesis by

Jun Young Jang

Professor: Se Won Suh

A Thesis Submitted to the Graduate Faculty of Seoul National University in Partial Fulfillment of the Requirements for the Degree of Doctor of Philosophy

2016

Abstract

Peroxisome proliferator-activated receptor γ (PPARγ) is a member of the nuclear receptor superfamily. It functions as a ligand-activated transcription factor and plays important roles in the regulation of adipocyte differentiation, type 2 diabetes mellitus, and inflammation. Many PPARγ agonists bind to the canonical ligand-binding pocket near the helix H12. More recently, an alternate ligand-binding site of the PPARγ ligand-binding domain (LBD) was identified; it is located beside the Ω loop between the helices H2′ and H3. Previously it was reported that the chirality of two optimized enantiomeric PPARγ ligands (S35 and R35) differentiates their PPARγ transcriptional activity, binding affinity, and inhibitory activity toward Cdk5 (cyclin-dependent kinase 5)-mediated phosphorylation of PPARγ at Ser273. S35 is a PPARγ phosphorylation inhibitor with promising glucose uptake potential, while R35 behaves as a potent conventional PPARγ agonist. To provide a structural basis for understanding the differential activities of these ligands, I have determined crystal structures of the PPARγ LBD in complex with either S35 or R35. These structural data reveal a significant difference in the binding modes of these enantiomeric ligands to the PPARγ LBD. S35

occupies the alternate ligand-binding site, whereas R35 binds to the canonical ligand-binding pocket, thus explaining their different behaviors as PPARγ agonists. This finding provides a useful platform for the development of a new generation of PPARγ ligands as anti-diabetic drug candidates.

Helicobacter pylori infection is one of the highest risk factors for gastroduodenal diseases including gastric cancer. Tumor necrosis factor-α (TNF-α) is one of the essential cytokines for tumor promotion and thus a *H. pylori* protein that induces TNF-α is believed to play a significant role in gastric cancer development in humans. The *HP0596* gene product of *H. pylori* strain 26695 was identified as the TNF-α inducing protein (Tipα). Tipα is secreted from *H. pylori* as dimers and enters the gastric cells. It was shown to have a DNA binding activity. Here I have determined the crystal structure of Tipα from *H. pylori.* Its monomer consists of two structural domains ("mixed domain" and "helical domain"). Tipα exists as a dimer in the crystal and the dimeric structure represents a novel scaffold for DNA binding. A positively-charged surface patch formed across the two monomers of the Tipα dimer by the loop between helices α1 and α2 may be important in DNA binding.

Keywords: crystal structure / S35 / R35 / alternate ligand-binding site / Ω loop / peroxisome proliferator-activated receptor / type 2 diabetes / PPARγ agonist / tumor necrosis factor-α inducing protein / Tipα / HP0596 / *Helicobacter pylori* / gastric cancer

Table of Contents

Abstract · · ·

Chapter 1. Structural basis for differential transcription activation by enantiomeric agonists of PPARγ

1.1 Introduction · · ·

Chapter 2. Crystal structure of the TNF-α inducing protein (Tipα) from *Helicobacter pylori*: Insights into its DNA binding activity

2.1 Introduction · · ·

List of Tables

Chapter 1.

Table 1-1. Data collection statistics · 17

Table 1-2. Refinement statistics · 18

Chapter 2.

Table 2-1. Data collection and phasing statistics · · · · · · · · · · · · · · · · · 72

Table 2-2. Refinement statistics · 75

List of Figures

Chapter 1.

Figure 1-1. LBP-sizes and shapes of classical and adopted nuclear receptor · · ·

Chapter 2.

Figure 2-1. Sequence alignment of *H. pylori* Tipα and its homologs, and secondary structure assignment of HP0596 · · · · · · · · · · · · 64

Figure 2-2. Schematic illustration for the carcinogenic role of *H. pylori* Tipα· 65

Figure 2-3. A crystal of *H. pylori* Tipα · 71

Figure 2-4. Structure of *H. pylori* Tipα monomer · · · · · · · · · · · · · · · · · · 78

Figure 2-5. Topology diagram of *H. pylori* Tipα monomer · · · · · · · · · · · · 79

Figure 2-6. Structure of *H. pylori* Tipα dimer · 82

Figure 2-7. Surface electrostatic potential of *H. pylori* Tipα dimer · · · · · · · 83

Figure 2-8. Structural comparison of *H. pylori* Tipα with the structure of Nab2 · · · · · · · · · · · · · · · · · · ·

Abbreviations

PPAR	peroxisome proliferator-activated receptor
LBD	ligand-binding domain
LBP	ligand-binding pocket
TZD	thiazolidinedione
Cdk5	cyclin-dependent kinase 5
SRC1	steroid receptor coactivator-1
r.m.s.	root mean square
TNF-α	tumor necrosis factor-alpha
Tipα	TNF-α-inducing protein
MAD	multiwavelength anomalous diffraction
SeMet	selenomethionine
PDB	Protein Data Bank
NTD	N-terminal domain
dsDNA	double-stranded DNA

Chapter 1

Structural basis for differential transcription activation by enantiomeric agonists of PPARγ

1.1. Introduction

Peroxisome proliferator-activated receptors (PPARs) are a group of ligand-activated transcription factors that belongs to the thyroid hormone receptor-like nuclear receptor (NR) subfamily 1 (Gallastegui et al., 2015). PPARs bind to cognate peroxisome proliferator response elements (PPREs) through hetero-dimerization with retinoid X receptors (RXRs) and regulate the transcription of target genes (Berger and Moller, 2002). Among three known mammalian PPAR subtypes (PPARα, PPARγ, and PPARδ/β) that show distinct ligand specificity and tissue distribution, PPARγ is highly expressed in adipocytes and macrophages (Tontonoz et al., 1994; Ricote et al., 1998). It plays essential roles in adipocyte differentiation, glucose

homeostasis, lipid metabolism, insulin sensitization, and inflammatory action (Lehrke and Lazar, 2005). Thus, PPARγ is a potential therapeutic target for metabolic syndrome and inflammatory diseases such as type 2 diabetes and atherosclerosis (Walczak and Tontonoz, 2002; Waku et al., 2010).

Like other nuclear receptors, PPARγ contains an N-terminal domain (NTD), a DNA-binding domain (DBD), a hinge region, and a ligand-binding domain (LBD). The LBD of PPARγ is comprised of 12 α-helices in a three-layer sandwich and a small four-stranded β-sheet. The canonical ligand-binding pocket (LBP) of PPARγ is a Y-shaped hydrophobic cavity within the 12 helix-bundle of LBD. Its volume is in the range of 1,200-1,450 $Å^3$, which is much larger than those of most other nuclear receptors (Gallastegui et al., 2015; Nolte et al., 1998; Waku et al., 2010). In the apo form of the PPARγ LBD, helix 12 (H12), a highly flexible switch element, is in a state of equilibrium among many different conformations varying from active to inactive (Kallenberger et al., 2003). Binding of PPARγ agonists in the canonical LBP induces conformational changes in the LBD via the formation of a hydrogen bond network that stabilizes H12 (Nolte et al., 1998). Binding of agonists also affects the recruitment of coactivators (Nolte et al., 1998) or corepressors (Hu et al., 2001), which is a key mechanism for modulating target gene expression. In addition to the canonical LBP near H12, an

alternate ligand-binding site was identified in the LBD of PPARγ adjacent to the Ω loop between helices H2′ and H3 (Waku et al., 2010; Hughes et al., 2014).

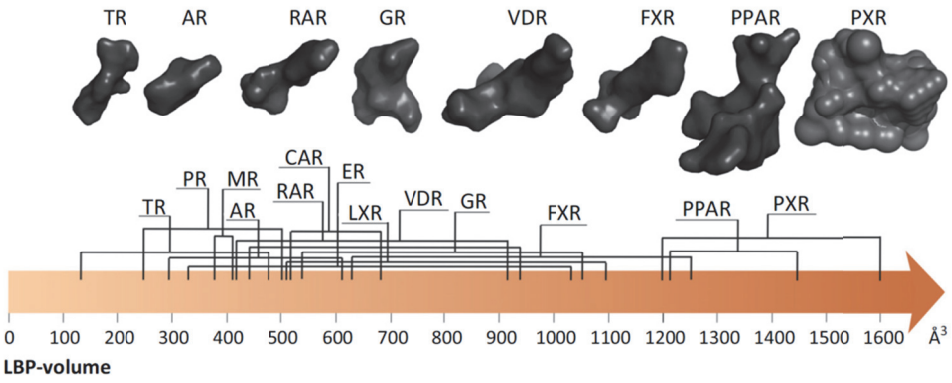

Figure 1-1. LBP-sizes and shapes of classical and adopted nuclear receptors. [Gallastegui et al. (2015) *Trends Biochem. Sci.* **40(1)**, 25-35]

The canonical LBP of PPARγ can accommodate a multitude of endogenous and synthetic ligands and also simultaneously more than one PPARγ ligand (Bruning et al., 2007; Xu et al., 2008; Loiodice et al., 2011; Hughes et al., 2014). The large ligand-binding pocket of PPARγ is likely to have a role in its biology by allowing the receptor to perceive not only a single ligand but rather a pool of related ligands (Waku et al., 2010; Itoh et al., 2008). This means that the concentration of this pool of ligands is likely to be more relevant than the concentration of each individual ligand, making PPARγ a sensor of oxidized fatty acids (Itoh et al., 2008).

Synthetic ligands of PPARγ include a class of insulin-sensitizing anti-diabetic drugs referred to as thiazolidinediones (TZDs), such as rosiglitazone and pioglitazone, and the GW series of L-tyrosine analogs (Ambrosio et al., 2007). Despite the clinical benefit of TZDs, their use has been associated with adverse effects, including weight gain, increased adipogenesis, renal fluid retention, plasma volume expansion and possible increased incidences of cardiovascular events (Berger et al., 2005; Nissen and Wolski, 2007; Bruning et al., 2007). Rosiglitazone and pioglitazone, PPARγ TZD full agonists, are structurally similar but afford different clinical adverse events. It indicates that subtle changes in the ligand-receptor interaction can lead to differences in the pharmacology of the TZD drugs. This highlights the

importance of the need for a more complete understanding of the mechanism of PPARγ modulation by synthetic ligands (Bruning et al., 2007).

It was reported that synthetic PPARγ ligands exert another biochemical function by blocking the phosphorylation of PPARγ at Ser273 by cyclin-dependent kinase 5 (Cdk5) (Choi et al., 2010). The phosphorylation of PPARγ does not alter its adipogenic capacity but leads to dysregulation of the genes whose expression is altered in obesity, including lowered expression of the insulin-sensitizing adipokine, adiponectin (Choi et al., 2010). The Cdk5-mediated phosphorylation of PPARγ is blocked by anti-diabetic PPARγ ligands, such as rosiglitazone (a full agonist) and MRL24 (a partial agonist) (Choi et al., 2010). Inhibition of PPARγ phosphorylation in obese patients by rosiglitazone is very tightly associated with the anti-diabetic effects of this drug (Choi et al., 2010). We previously identified two optimized enantiomeric PPARγ ligands (R35 and S35) and reported that the chirality of these enantiomeric ligands differentiates their PPARγ transcriptional activity, binding affinity, and inhibitory activity toward Cdk5-mediated phosphorylation of PPARγ at Ser273. S35, a partial agonist of PPARγ, shows an inhibitory activity toward Cdk5-mediated phosphorylation of PPARγ at Ser273 with promising glucose uptake potential, whereas its

enantiomer R35 is a highly potent conventional PPARγ agonist (Koh et al., 2014 Angew. Chem. Int. Ed.).

To provide a structural basis for understanding their differential activities, we have determined crystal structures of the PPARγ LBD in complex with either S35 or R35. Unexpectedly, these enantiomeric ligands bind to the PPARγ LBD in significantly different manners. The partial agonist S35 occupies the alternate site near the Ω loop, whereas the full agonist R35 binds entirely to the canonical LBP near the helix H12. The flexible Ω loop region is stabilized by the binding of S35 in the alternate site. The S35-bound PPARγ LBD simultaneously accommodates a fatty acid (modeled here as myristate) in the canonical LBP. In contrast, the fatty acid binding is prohibited by the binding of R35 to the PPARγ LBD. This study shows that different binding modes of S35 and R35 in the PPARγ LBD determine their differential behaviors as PPARγ agonists. This finding may lead to the development of a new generation of anti-diabetic drugs that target PPARγ.

1.2. Material and methods

1.2.1. Protein expression and purification

The gene encoding the human PPARγ LBD construct (residues 195–477 in PPARγ1 numbering) was PCR-amplified using a human cDNA clone encoding PPARγ (clone ID: hMU000317) as the template, which was provided by the Korea Human Gene Bank, Medical Genomics Research Center, Korea Research Institute of Bioscience & Biotechnology. It was cloned into the expression vector pET-28b(+) (Novagen). This construct of the recombinant protein encodes a 21-residue N-terminal tail (MGSSHHHHHH SSGLVPRGSH M) containing a His_6 tag and a thrombin cleavage site in front of the starting residue Ala195 (PPARγ1 numbering). The recombinant human PPARγ LBD was overexpressed in *Escherichia coli* Rosetta 2(DE3) cells using the Luria Broth culture medium. Protein expression was induced by 0.5 mM isopropyl β-D-thiogalactopyranoside and the cells were incubated for additional 24 h at 18°C following growth to mid-log phase at 37°C. The cells were lysed by sonication in buffer A [20 mM Tris-HCl at pH 8.5, 150 mM NaCl, 10% (v/v) glycerol and 0.1 mM tris(2-carboxyethyl) phosphine hydrochloride] containing 5 mM imidazole and 1 mM phenylmethylsulfonyl fluoride. The crude lysate was centrifuged

at 36,000 g for 1 hr. The supernatant was applied to a HiTrap Chelating HP affinity chromatography column (GE Healthcare), which was previously equilibrated with buffer A containing 5 mM imidazole. Upon eluting with a gradient of imidazole in the same buffer, the human PPARγ LBD was eluted at 45–100 mM imidazole concentration. The eluted protein was desalted in buffer A by HiPrep 26/10 desalting column (GE Healthcare) to remove imidazole, and the protein was cleaved with 2 units of thrombin (Sigma Aldrich) per mg of the PPARγ LBD at 4°C overnight. Both the N-terminal fusion tag and the uncleaved protein were removed by affinity chromatography with a HiTrap Chelating HP affinity chromatography column. The flow-through was applied to a HiLoad XK-16 Superdex 200 prep-grade column (GE Healthcare), which was previously equilibrated with buffer A. Fractions containing the human PPARγ LBD were pooled and concentrated to 15.4 mg ml^{-1} using an Amicon Ultra-15 Centrifugal Filter Unit (Millipore).

1.2.2. Crystallization

Before crystallization, the purified PPARγ LBD and a LXXLL motif-containing peptide derived from human steroid receptor coactivator-1 (SRC1) (residues 685–700, ERHKILHRLLQEGSPS) were mixed in a molar ratio of 1:2, in the presence or absence of a 10-fold molar excess of the PPARγ ligand S35 or R35. After overnight incubation, the protein-ligand complexes were crystallized by the sitting-drop vapor diffusion method using the Mosquito robotic system (TTP Labtech) at 23°C by mixing 0.2 μl of the protein solution and 0.2 μl of the reservoir solution. The PPARγ·SRC1 crystals (Figure 1-2) and the PPARγ·S35·SRC1 crystals were obtained with a reservoir solution of 2.2 M sodium malonate at pH 7.0. The initial PPARγ·S35·SRC1 crystals appeared as multiple crystals that were not suitable for diffraction and, therefore, microseeding technique was used to obtain single crystals. Several pieces of the crystals were transferred into an Eppendorf tube containing a Seed Bead (Hampton Research) and 50 μl stabilization solution of 2.2 M sodium malonate at pH 7.0, and were vortexed to produce microseeds. The stock solution of microseeds was then briefly centrifuged and diluted serially by a factor of 100–1000 in the same stabilization solution. Each sitting drop was prepared by mixing the protein

solution, the reservoir solution, and the microseed solution in a volume ratio of 1:0.7:0.3. Single crystals (Figure 1-3) grew reproducibly to dimensions of approximately 0.35 × 0.2 × 0.1 mm within a few days. The PPARγ·R35·SRC1 crystals (Figure 1-4) were obtained with a reservoir solution of 57.5% (v/v) Tacsimate at pH 7.0.

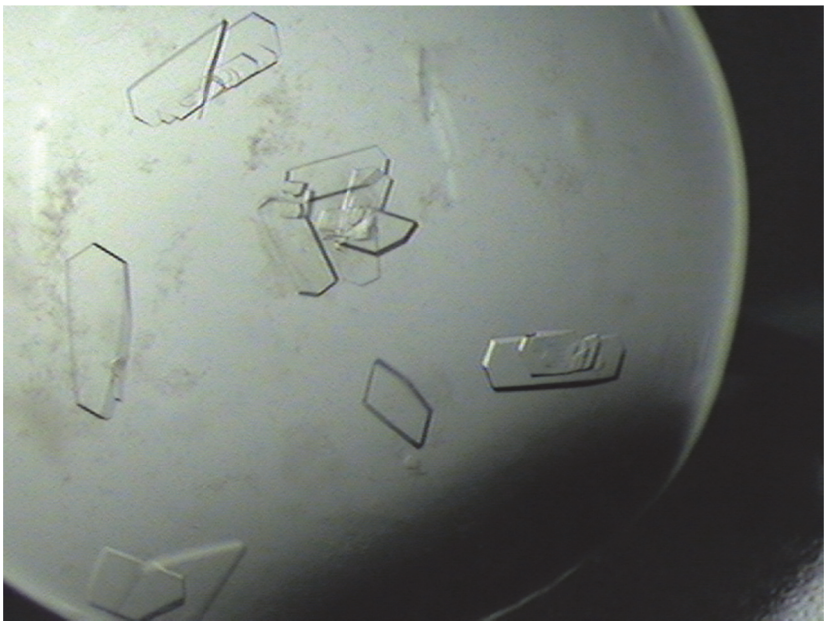

Figure 1-2. Crystals of the PPARγ·SRC1 complex.

Their approximate dimensions are 0.35 mm × 0.2 mm × 0.1 mm.

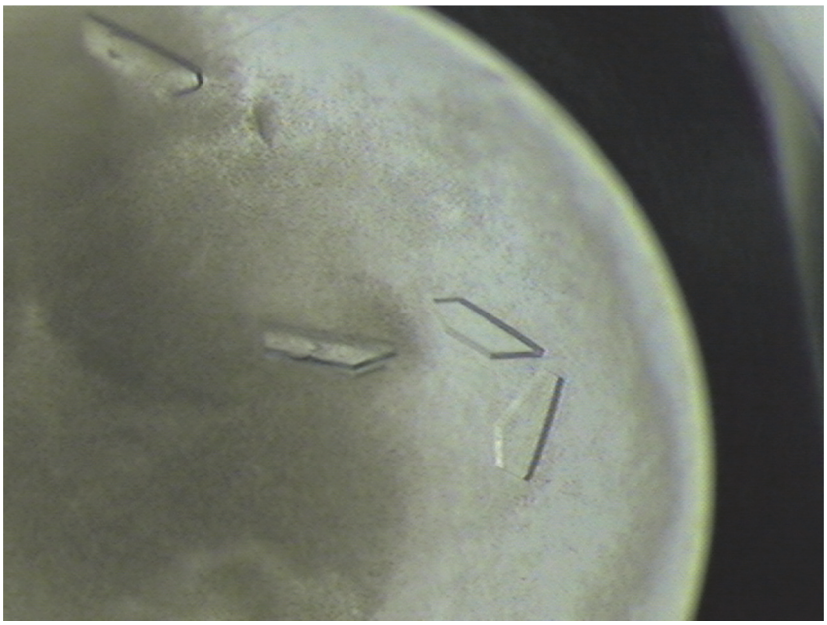

Figure 1-3. Crystals of the PPARγ·S35·SRC1 complex.

Their approximate dimensions are 0.35 mm × 0.2 mm × 0.1 mm.

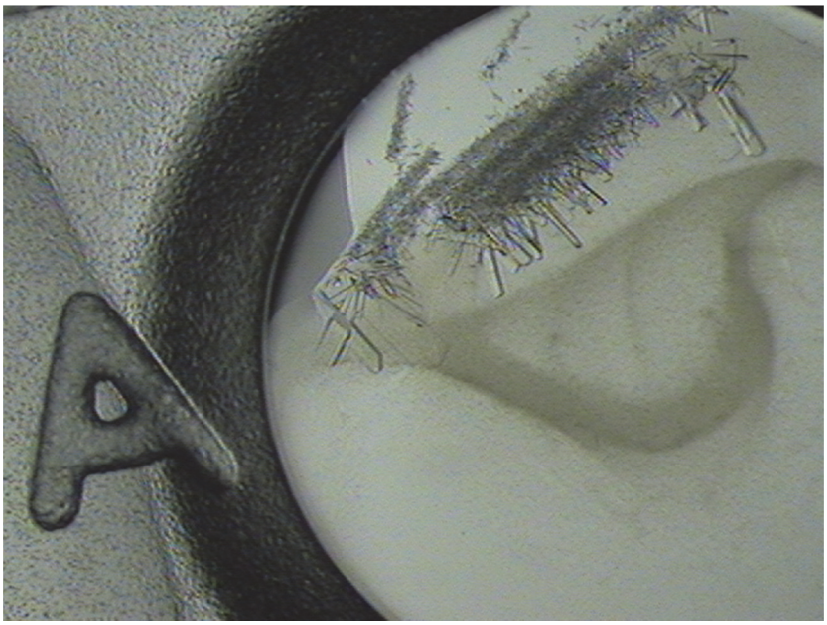

Figure 1-4. Crystals of the PPARγ·R35·SRC1 complex.

Their approximate dimensions are 0.2 mm × 0.1 mm × 0.1 mm.

1.2.3. X-ray data collection, structure determination, and refinement

All sets of X-ray diffraction data except for the S35-bound PPARγ LBD were collected at 100 K using a Quantum Q270 CCD detector system (Area Detector Systems Corporation, Poway, California) at the BL-7A experimental station of Pohang Light Source, Korea. The X-ray data from the crystal of S35-bound PPARγ LBD were collected at 100 K using a Quantum 315r CCD detector system (Area Detector Systems Corporation, Poway, California) at the BL-5C experimental station of Pohang Light Source, Korea. Raw X-ray diffraction data were processed and scaled using the program suit *HKL2000* (Otwinowski and Minor, 1997). Data collection statistics are summarized in Table 1-1. All structures were solved by molecular replacement with the program *MolRep* (Vagin and Teplyakov, 2010) using the previously published PPARγ LBD structure (PDB code, 3VN2; Amano et al., 2012) as a search model. Subsequent model building was done manually using the program *COOT* (Emsley et al., 2010) and the models were refined with the program *REFMAC5* (Murshudov et al., 1997), including the bulk solvent correction. A total of 5% of the data was randomly set aside as test data for the calculation of R_{free} (Brünger et al., 1992). The stereochemistry of the refined models was assessed by

MolProbity (Chen et al., 2010). Refinement statistics are summarized in Table 1-2.

Table 1-1. Data collection statistics

Data collection			
Model name	Agonist-free	S35-bound	R35-bound
X-ray wavelength (Å)	0.9793	1.0000	1.0000
Space group	$P2_12_12$	$P2_12_12$	$P2_12_12$
Unit cell parameters			
a (Å)	131.31	131.82	131.65
b (Å)	53.06	53.29	52.45
c (Å)	53.55	53.74	54.29
$\alpha = \beta = \gamma$ (°)	90	90	90
Resolution range (Å)	50–2.35 (2.39–2.35)[a]	50–2.10 (2.14–2.10)[a]	50–1.85 (1.88–1.85)[a]
Total / unique reflections	94,500 / 16,193	128,674 / 22,810	156,963 / 32,794
Completeness (%)	99.4 (100.0)[a]	99.5 (100.0)[a]	99.7 (100.0)[a]
$\langle I \rangle / \langle \sigma_I \rangle$	36.2 (4.0)[a]	41.1 (3.6)[a]	39.5 (3.0)[a]
R_{merge}[b] (%)	7.4 (60.3)[a]	6.7 (59.1)[a]	4.2 (43.7)[a]

Footnotes to Table 1-1

[a] Values in parentheses refer to the highest resolution shell.

[b] $R_{merge} = \Sigma_h\Sigma_i \mid I(h)_i - \langle I(h) \rangle \mid / \Sigma_h\Sigma_i I(h)_i$, where $I(h)$ is the intensity of reflection h, Σ_h is the sum over all reflections, and Σ_i is the sum over i measurements of reflection h.

Table 1-2. Refinement statistics

Model refinement			
Mocdel name	Agonist-free	S35-bound	R35-bound
Resolution range (Å)	30–2.35	30–2.10	30–1.85
R_{work} / R_{free}[a] (%)	21.1 / 25.7	21.2 / 24.2	20.6 / 22.8
No. of non-hydrogen atoms			
Protein	2,196	2,245	2,260
Ligand	22	67	45
Water oxygen	45	108	211
Average *B* factor (Å^2)			
Protein	68.0	54.7	39.0
Ligand	96.6 (99.8)[b]	77.2 (78.9)[b]	29.3 (-)[b]
Water oxygen	59.4	56.6	44.9
R.m.s. deviations from ideal geometry			
Bond lengths (Å)	0.012	0.011	0.011
Bond angles (°)	1.49	1.49	1.48
Ramachandran plot[c]			
Favored / Outliers (%)	97.4 / 0	98.2 / 0	99.3 / 0
Poor rotamers (%)	0	0	0

Footnotes to Table 1-2

[a] $R_{work} = \Sigma \mid |F_{obs}| - |F_{calc}| \mid / \Sigma |F_{obs}|$, where R_{free} is calculated for a randomly chosen 5% of reflections, which were not used for structure refinement and R_{work} is calculated for the remaining reflections.

[b] Values in parentheses refer to the average *B* factor of myristate. In the case of R35, myristate binding is blocked by R35. For other data, extra electron

density was modeled as myristate.

[c] Values obtained using *MolProbity*.

1.2.4. In vitro kinase assay

In vitro Cdk5 assay was conducted according to the manufacturer's instruction (Cell Signaling Technology). Briefly, 0.5 μg of the purified PPARγ LBD was incubated with active Cdk5/p35 (Millipore) in assay buffer (25 mM Tris-HCl at pH 7.5, 5 mM β-glycerophosphate, 2 mM dithiothreitol, 0.1 mM Na_3VO_4, 10 mM $MgCl_2$) containing 25 μM ATP for 30 min at 30°C. S35 and R35 were pre-incubated with the PPARγ LBD for 30 min at 30°C before performing the assay. The Rb-peptide (residues 773–928, Millipore) was also used as a substrate of Cdk5 to test whether the compounds affect the kinase activity of Cdk5 or not. Phosphorylation of the Cdk5 substrates was analyzed by Western blotting with an anti-Cdk substrate antibody to detect phospho-Ser in a K/R-S-P-K/R motif, which is the consensus motif for Cdk substrates (Cell Signaling Technology).

1.2.5. Cell-based luciferase reporter gene assay

The transcriptional activity of human PPARγ was determined by measuring the luciferase activity in PPARγ reporter assays (Indigo Biosciences, State College, PA) according to the manufacturer's instruction. The reporter cells, derived from Chinese hamster ovary cells, constitutively express human hybrid PPARγ. These reporter cells incorporate a responsive luciferase reporter gene and quantifying expressed luciferase activity provides a sensitive detection of PPARγ activity in the system. Briefly, 100 µl of human PPARγ reporter cell suspensions was dispensed into the wells of 96-well assay plates and 100 µl of test compounds was added to the respective wells in triplicates. Plates were transferred into a 37°C, humidified 5% CO_2 incubator for 22 h. Control cells were treated with 0.1% (v/v) DMSO in a compound-screening medium. For studies involving the covalent antagonist GW9662, before incubation with PPARγ ligands S35 and rosiglitazone, cells were first pre-incubated with 5 µM GW9662 for 3 h. At the end of the treatment, the medium was discarded and 100 µl of Luciferase Detection Reagent was added to each well of the assay plate. The reaction mixture was incubated for 15 min at room temperature and luminescence was quantified using a Bio-Tek microplate reader (ELx800TM,

Bio-Tek Instruments Inc.). Fold changes of treated cells over DMSO-treated control cells were plotted in triplicates.

1.3. Results

1.3.1. Overall structure of the PPARγ LBD and structural comparisons

Here I have solved the crystal structures of the PPARγ LBD complexed with either S35 or R35 (Figure 1-5) in the presence of a peptide derived from the human steroid receptor coactivator-1 (SRC1) coactivator protein. I have also solved the agonist-free structure of the PPARγ LBD in the presence of the SRC1 coactivator peptide. The structures reveal the canonical nuclear receptor fold, comprised of three-layered antiparallel α-helices and a four-stranded β-sheet. The C-terminal activation function-2 (AF-2) helix (H12) exists in the active conformation. The LXXLL motif of SRC-1 coactivator is in a helical conformation and is bound in the hydrophobic cleft between the charge clamp, which is formed by Glu471 and Lys301 on the surface of the PPARγ LBD (Figure 1-6A) (Nolte et al., 1998). The structures of the PPARγ LBD complexed with either S35 or R35 are very similar to that of the agonist-free structure, with an r.m.s. deviation of 0.49 Å or 0.58 Å for 261 Cα atom pairs. The r.m.s. deviation between the structures of the two complexes is slightly larger (1.01 Å for 265 Cα pairs) (Figure 1-6B). Interestingly, a large Cα r.m.s. deviation (4.80 Å) occurs between residues

Lys261 and Thr268, which belong to the flexible Ω loop. This region is reasonably well-defined by the electron density in both complexes and the observed large structural difference around this region is a consequence of different binding modes of S35 and R35.

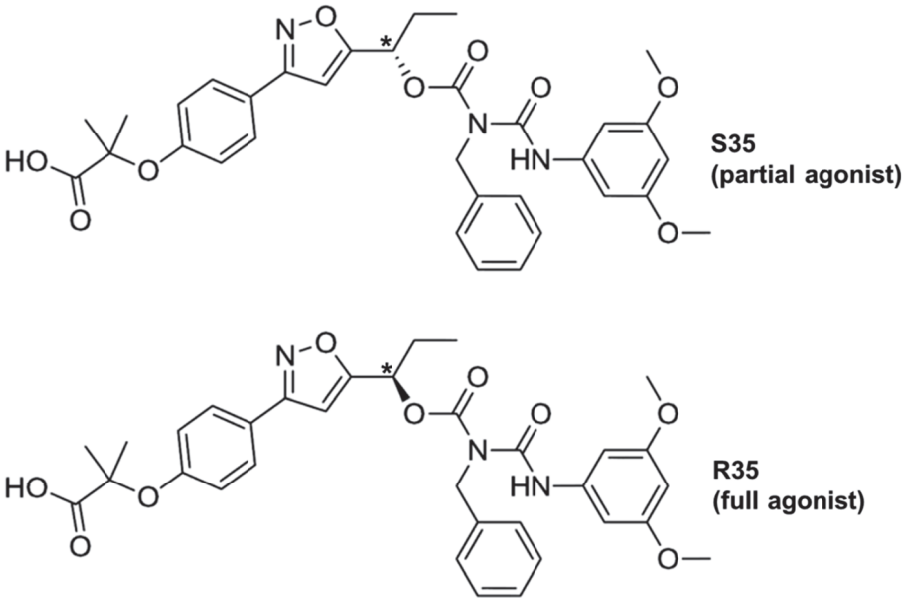

Figure 1-5. Chemical structures of S35 and R35.

The chiral center is marked with an asterisk.

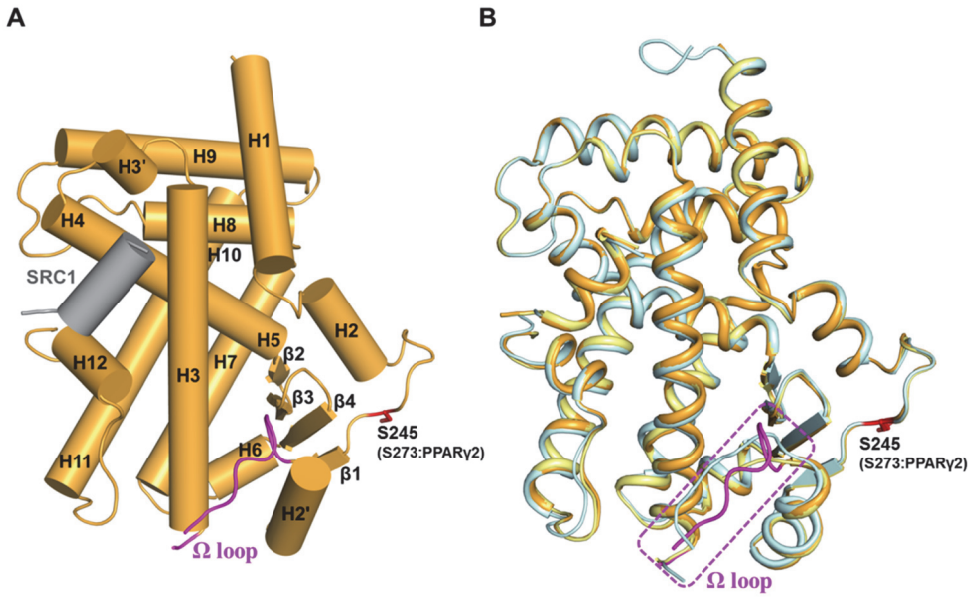

Figure 1-6. Overall structure of the LBD of PPARγ.

(A) Cylinder diagram (α-helices represented by cylinders) of the S35-bound PPARγ LBD (bright orange) with SRC1 coactivator peptide (grey), with the secondary structure elements labeled. The Ω loop between helices H2' and H3 is colored in violet. The bound partial agonist S35 is not shown. (B) Superposition of PPARγ LBD structures of agonist-free (pale yellow), S35-bound (bright orange), and R35-bound (pale cyan) models, all of which include the SRC1 coactivator peptide. The phosphorylation site at Ser245 (red) is represented by sticks (Ser245 of PPARγ1 corresponds to Ser273 of

PPARγ2). Only the Ω loop of S35-bound LBD is colored in violet. Agonist ligands are not shown.

1.3.2. S35 occupies the alternate ligand binding site in the PPARγ LBD

The electron density of S35 in the PPARγ ligand binding pocket is interrupted at the central moiety of the molecule, but it is generally well defined (Figure 1-7A and 1-8A). Recently Hughes et al. reported the alternate ligand-binding site of the PPARγ LBD which was previously irrelevant to the ligand binding. Interestingly, S35 is bound to the alternate ligand-binding site by wrapping around helix 3, and is surrounded by β-sheet and the Ω loop. A comparison between structures of S35 and rosiglitazone (2PRG) complexes revealed that a small portion of the molecules is overlapped. And also S35 is located in the opposite direction compared with the R counterpart and the dimethoxyphenyl ring and the carbamoyl group of the two enantiomers are overlapped with each other (Figure 1-9). S35 is far from the canonical ligand-binding pocket and shows no direct hydrogen bond interactions with the AF2 helix. The interactions between the PPARγ LBD and S35 involve two hydrogen bonds and some hydrophobic interactions (Figure 1-7B). The carboxylate group of S35 participates in hydrogen bonds. One of the carboxylate oxygens forms a hydrogen bond with the backbone amino group of Leu270 with a distance of 2.67 $Å^2$. The other carboxylate oxygen is also hydrogen bonded with the Nε2 atom of Gln283 with a distance of 3.35 $Å^2$. The hydrophobic interactions of S35 with

the LBD can be divided into two groups. The first group is formed by the interactions to the the dimethoxyphenyl ring. This moiety occupies the space between helix 3 and β-sheet, which formed by residues of Ile281, Leu340, Ile341, and Met364. The second group is made up of interactions between the other parts of S35 and the LBD. This moiety is located in the alternate ligand-binding site of the LBD formed by residues Leu255, Gln259, Ile262, Phe264, Ile267, Thr268, Pro269, Arg280, Gly284, Phe287, and Ser342. We have observed the S35-bound PPARγ LBD structure and found two extra electron densities. The one is located near the AF2 helix. This region was occupied by the thiazolidinedione group in the rosiglitazone-bound structure. We assume that this electron density is a glycerol molecule comes from protein purification step. The other is placed between the helices 3 and 5 (Figure 1-10A). We guess that the second electron density is a long-chain fatty acid (Myristate) simultaneously bound in the PPARγ LBD as previous report (Puhl et al., 2012).

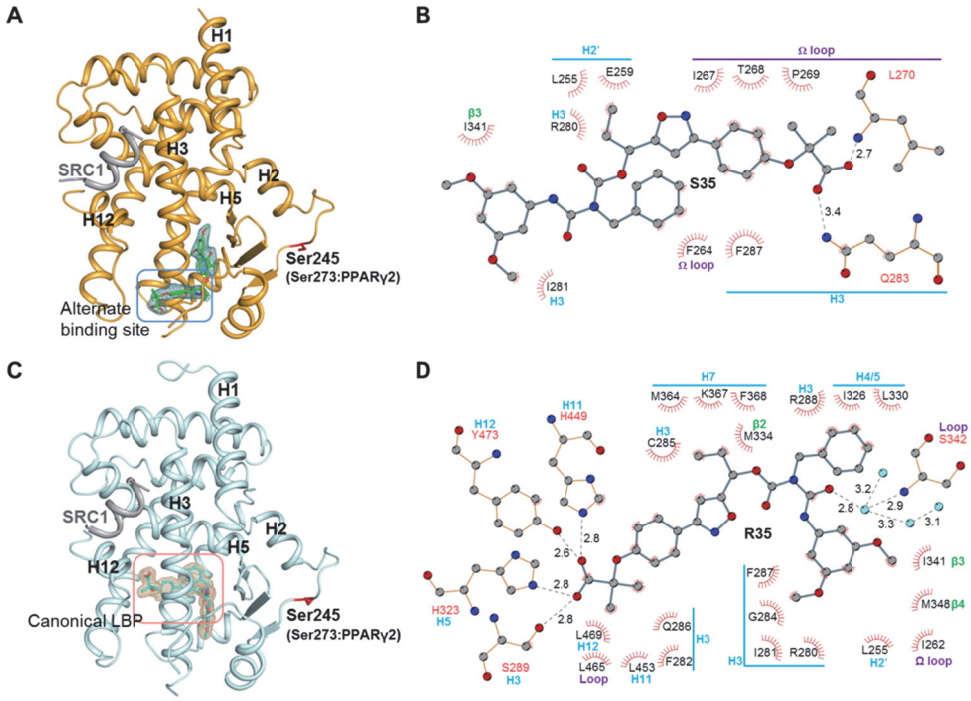

Figure 1-7. Structures of S35- and R35-bound PPARγ LBD.

(A) Ribbon diagram of the S35-bound PPARγ LBD (bright orange) with the SRC1 coactivator peptide (grey). The partial agonist S35, shown as a ball and stick model in green, occupies the alternate binding site of the PPARγ LBD. The electron density for S35 in the omit $mF_o - DF_c$ map is shown in light teal colored mesh (contoured at 2.0σ). The phosphorylation site at Ser245 (red) is represented by sticks. (B) Schematic representation of the interactions between the PPARγ LBD and S35, as calculated using

LIGPLOT. Hydrogen bonds are depicted by dashed lines, hydrophobic interactions are indicated by spoked arcs, and atoms with spokes. Oxygen atoms are colored red, nitrogen atoms blue, and carbon atoms grey. β: β-sheet (green). H: helix (cyan). Residue numbers correspond to PPARγ isoform 1. Hydrogen bonds are labeled with donor–acceptor distances in angstrom. (C) Ribbon diagram of the R35-bound PPARγ LBD (pale cyan) with the SRC1 coactivator peptide (grey). The conventional strong agonist R35, shown as a ball and stick model in cyan, binds to the canonical LBP of PPARγ LBD. The electron density for R35 in the omit $mF_o - DF_c$ map is shown in wheat colored mesh (contoured at 2.0σ). The phosphorylation site at Ser245 (red) is represented by sticks. (D) Schematic representation of the interactions between the PPARγ LBD and R35, as calculated using LIGPLOT. Hydrogen bonds are depicted by dashed lines, hydrophobic interactions are indicated by spoked arcs, and atoms with spokes. Oxygen atoms are colored red, nitrogen atoms blue, and carbon atoms grey. β: β-sheet (green). H: helix (cyan). Residue numbers correspond to PPARγ isoform 1. Hydrogen bonds are labeled with donor–acceptor distances in Ångström.

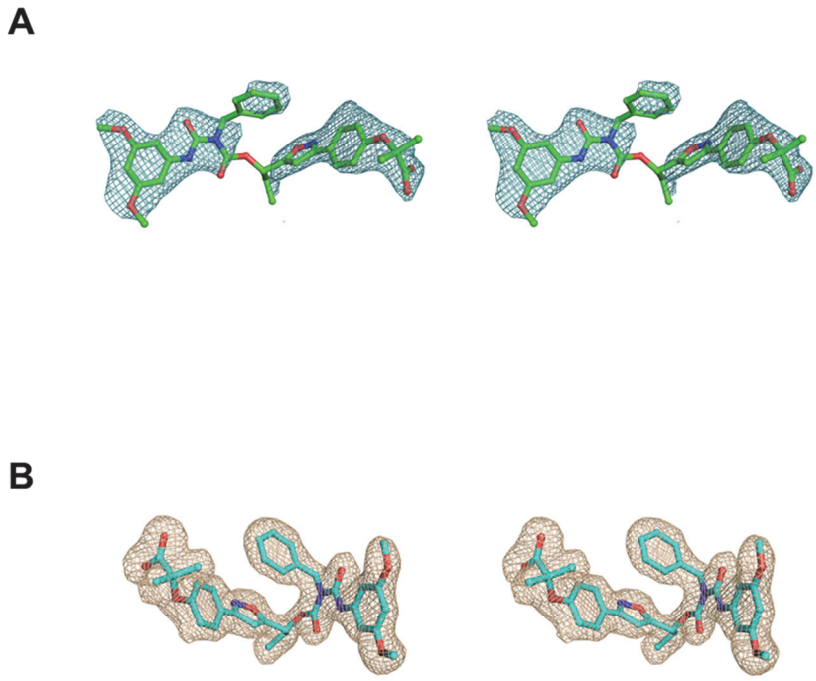

Figure 1-8. The omit $mF_o - DF_c$ electron density maps of S35 and R35.

(A) S35 shown in sticks (green) with electron density in light teal mesh (contoured at 2.0 σ). (B) R35 shown in sticks (cyan) with electron density shown in wheat mesh (contoured at 2.0 σ).

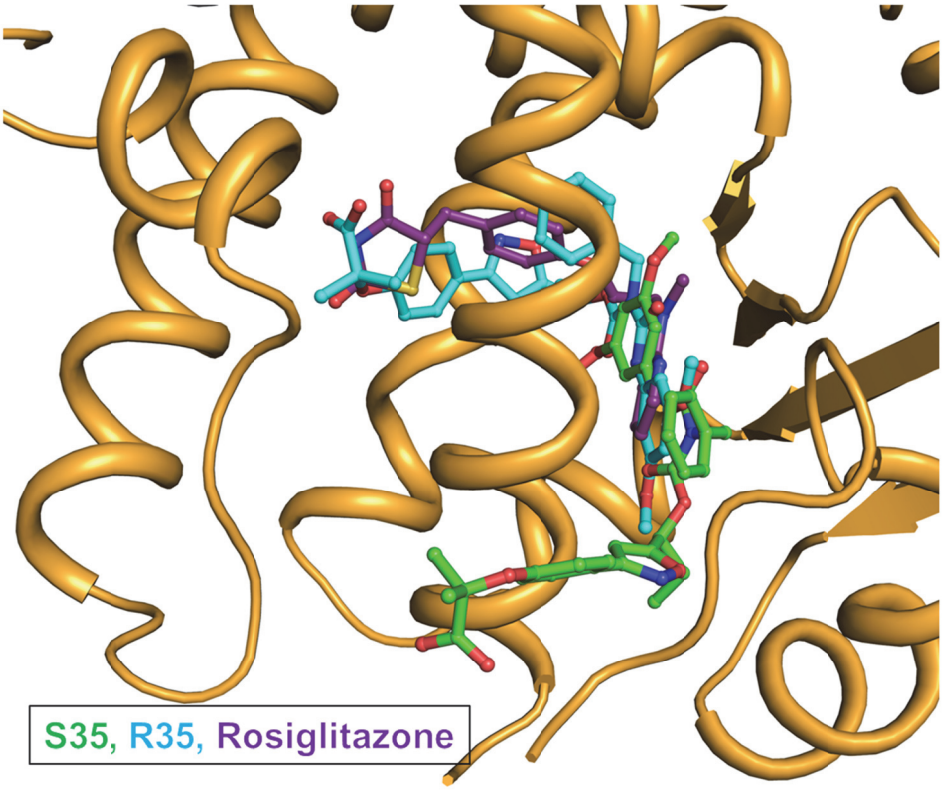

Figure 1-9. Superposition rosiglitazone-bound and R35-bound structures onto the S35-bound structure of PPARγ LBD.

Rosiglitazone-bound structure of PPARγ LBD (PDB ID: 2PRG) is colored in violet, the R35-bound structure in cyan, and the S35-bound structure in green.

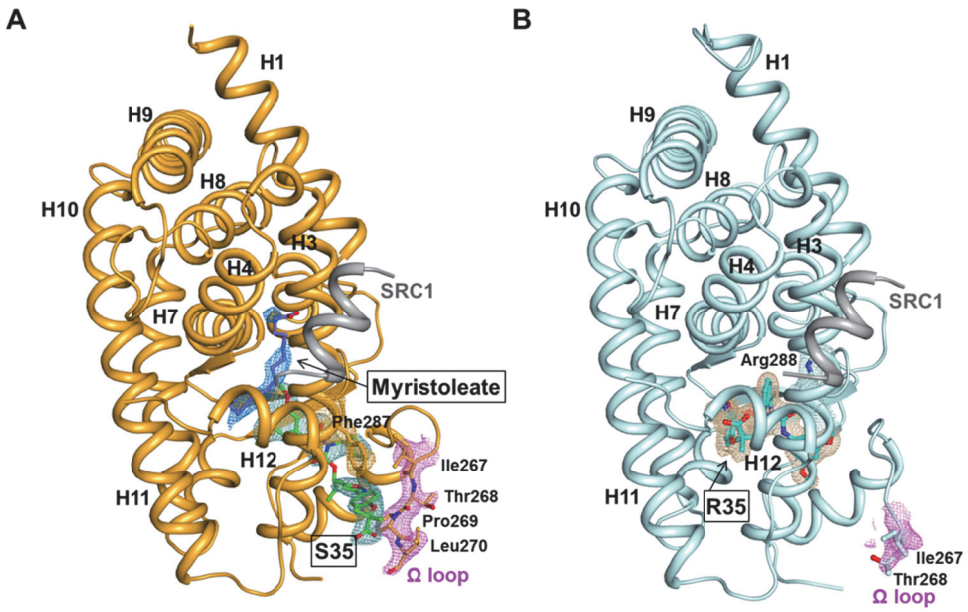

Figure 1-10. Side views of S35-bound and R35-bound PPARγ LBD.

(A) Side view of the S35-bound PPARγ LBD (bright orange) with SRC1 coactivator peptide (grey). The secondary structure elements are labeled. The Ω loop region is stabilized by S35 binding. Amino acid residues Ile267–Leu270 of the Ω loop are shown as sticks, with the $2mF_o - DF_c$ electron density map (violet) contoured at 1.0σ. The electron density for the partial agonist S35 in the omit $mF_o - DF_c$ map is also shown (contoured at 2.0σ). The electron density for the myristate (slate) in the omit $mF_o - DF_c$ map is shown in marine colored mesh (contoured at 2.0σ). (B) Side view of

the R35-bound PPARγ LBD (pale cyan) with SRC1 coactivator peptide (grey). The secondary structure elements are labeled. Amino acid residues Ile267 and Thr268 of the Ω loop are shown as sticks, with the $2mF_o - DF_c$ electron density map (violet) contoured at 1.0σ. The electron density for the conventional strong agonist R35 in the omit $mF_o - DF_c$ map is also shown (contoured at 2.0σ).

1.3.3. Ligand binding cavity of the PPARγ LBD in S35-bound structure

The ligand-binding pocket of the PPARγ LBD from the structure of S35 complex is a large Y-shaped cavity with a volume around 1560 $Å^3$ with three arms (Figure 1-11A). The left arm of the Y is composed of a mix of hydrophobic residues (Phe282, Ile326, Tyr327, Leu330, Val339, Leu353, Leu356, Phe360, Phe363, Met364, and Leu453) and polar residues (Cys285, Gln286, Ser289, His323, Lys367, and His449) and is covered by three residues from the AF-2 helix (Leu469 and Tyr473) and the loop between helices 11 and 12 (Leu465). The right arm of the Y is also formed by a mix of hydrophobic residues (Phe226, Pro227, Leu228, Ile296, Ile325, Met329, Leu333, Leu340, and Leu384) and polar residues (Arg288, Glu291, Glu395, Ser332, Glu343, and Asp381). The third arm of the Y-shaped pocket from the structure of S35 complex is extended beyond the alternate ligand-binding site which is approximately 200 $Å^3$ in volume. The third arm is composed of the hydrophobic residues Ile249, Leu255, Ile262, Phe264, Ile281, Ile341, and Met 348 and several polar residues Glu259, Arg280, and Ser342. The alternate ligand-binding site region is surrounded by the residues from helix 3 (Gln283 and Phe287) and the Ω loop between helices 2' and 3 (Ile267, Pro269, Leu270, and Lys275) (Figure 1-11A). One hundred twenty seven redundant crystal structures of the PPARγ LBD complexed with different

ligands that were taken from the PDB in February 2016 aligned with the S35-bound PPARγ LBD structure, all ligands were included in the Y-shaped pocket and S35 only occupied the alternate ligand-binding site (Figure 1-11B). As aforementioned, the presence of S35 inside the alternate ligand-binding site appears to induce a unique and stable conformation of the Ω loop, when compared with other published structures. Interestingly, the phenoxy ring of S35 forms a stacking interaction with two residues from helix 3 (Phe287) and the Ω loop (Pro269) (Figure 1-10A). In addition, from the B-factor analysis compared between S35-bound and Agonist-free, we observed that S35 binding induced the stabilization of helix 3 (Figure 1-12).

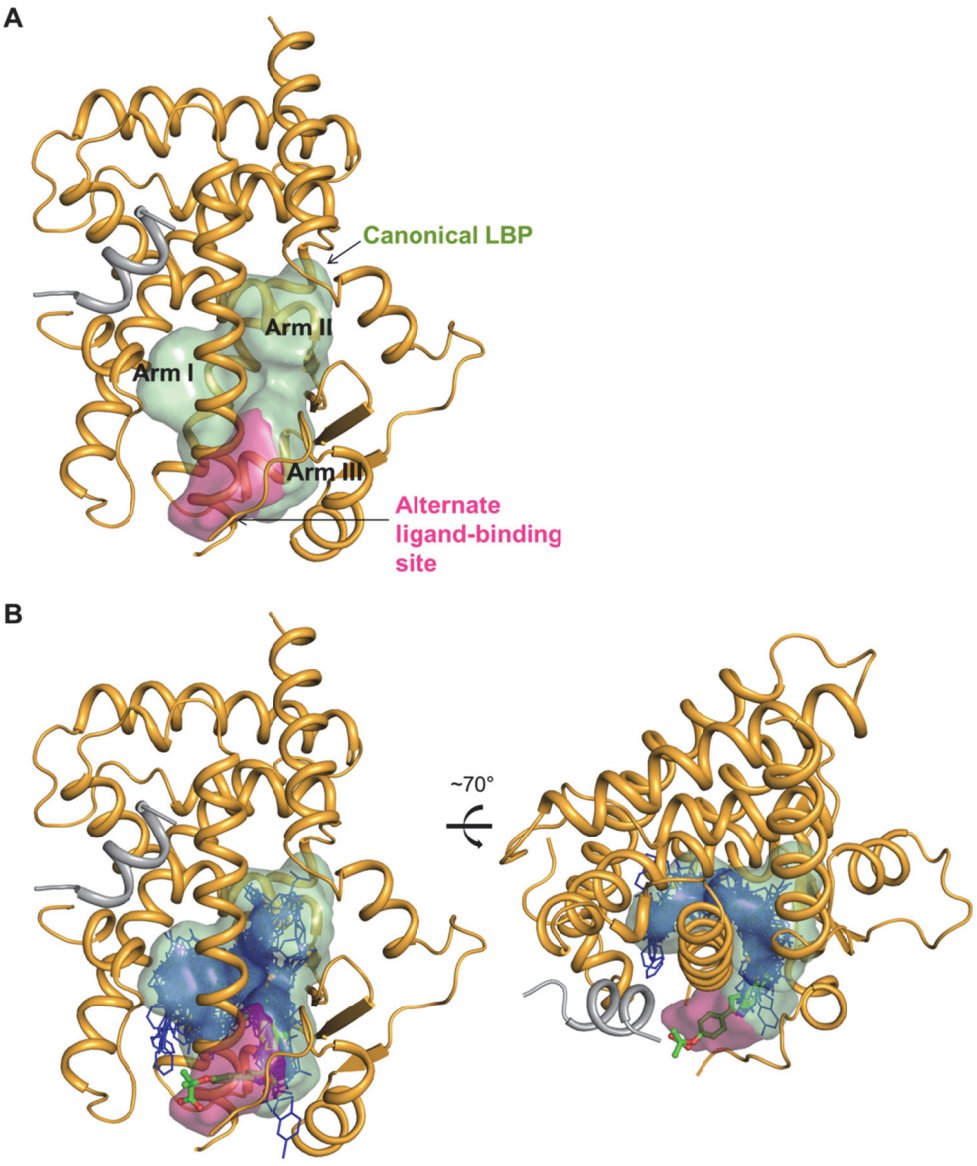

Figure 1-11. Ligand binding cavity of S35-bound PPARγ LBD.

(A) Ribbon diagram of S35-bound PPARγ LBD, with its ligand binding cavity shown as a surface and colored in pale green for the canonical LBP and in warm pink for the alternate binding site. The canonical Y-shaped cavity (pale green) has three arms and the alternate binding cavity (warm pink) extends from the base of Y. The cavity is calculated by the KVFinder program (Oliveira et al. 2014) using the values of step size (0.6 Å), probe in size (1.4 Å), and probe out size (4.5 Å). The total volume of the ligand binding cavity is approximately 1,560 $Å^3$, including the alternate binding site (200 $Å^3$). (B) Superposition of S35 and other reported PPARγ·ligand complexes with its ligand binding cavity in two different orientations. The ligand S35 (colored in green) occupies the alternate binding site of the PPARγ LBD, which is unique compared to many other previously-reported PPARγ ligands (colored in blue). The canonical ligand-binding cavity (colored in pale green) encompasses nearly all other PPARγ ligands except a few ligands. (A) S35 shown in sticks (green) with electron density in light teal mesh. (B) R35 shown in sticks (cyan) with electron density shown in wheat mesh.

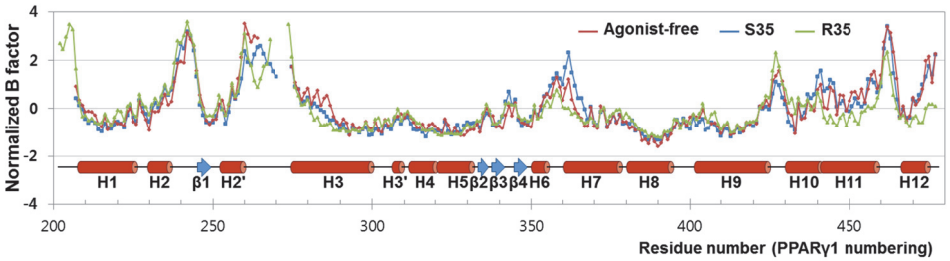

Figure 1-12. Normalized B factors of Cα atoms.

Agonist-free, S35-bound, and R35-bound PPARγ LBD structures show similar patterns as a function of the residue number. Secondary structure elements are also indicated.

1.3.4. R35 binds to the canonical LBP in the PPARγ LBD

The omit map calculated using the refined model revealed a clear electron density for R35 in the canonical LBP of the PPARγ LBD (Figure 1-7C and 1-8B). A comparison between structures of R35 and rosiglitazone (2PRG) complexes revealed that both ligands adopt a U-shaped conformation in the PPARγ LBD and wrap around Cys285 from helix 3 to directly contact AF-2 helix (Figure 1-9). Molecular volumes of R35 and rosiglitazone are 552 $Å^3$ and 315 $Å^3$, respectively (calculated by the Molinspiration web services at http://www.molinspiration.com/services/). The interactions between the PPARγ LBD and R35 involve two hydrogen bonding networks and numerous hydrophobic interactions (Figure 1-7D). The carboxyl group of R35 participates in a first hydrogen bonding network. One of the carboxylate oxygens makes a bifurcated hydrogen bond with the Oη atom of Tyr473 and the Nε atom of His449 with a distance of 2.58 $Å^2$ and 2.81 $Å^2$, respectively. The other carboxylate oxygen is also bifurcated hydrogen bonded with the Nε atom of His323 and the Oγ atom of Ser289 with a distance of 2.77 $Å^2$ and 2.85 $Å^2$, respectively. The other hydrogen bonding network occurs in a distant area from AF-2 helix. The oxygen of amide group of R35 forms a water mediated hydrogen bond with the main chain amide nitrogen of Ser342 of β-sheet. The hydrophobic interactions of

R35 with the LBD can be divided into four groups. The first group is formed by the interactions to the methylpropanoate moiety. This moiety is positioned in a hydrophobic region of the LBD pocket formed by the side chain of Phe282, Gln286, Leu453, and Leu469. The second group is the asymmetric carbon, isoxazole ring and phenoxy ring. This moiety is located in a narrow groove of the LBD formed by residues Cys285, Leu330, Met334, Met364, Lys367, and Phe368. The third group of interaction is formed between the benzyl ring of the ligand and the side chains of residues Arg288, Ile326, and Leu330. The benzyl ring of R35 particularly engaged in the CH-π interaction with the alkyl chain of Arg288 (Figure 1-10B). The forth group is made up of interactions between the dimethoxyphenyl ring and the LBD. This moiety occupies the space between helices 2' and 3 and β-sheet, which formed by residues of Leu255, Arg280, Ile281, Gly284, Phe287, and Ile341. Compared with other reported structures, both S35 and R35 stabilize the conformation of the Ω loop. The binding of R35 in the LBD induce the stable conformation of the Ω loop, although not as strong as the binding of S35 (Figure 1-10 and 1-12).

1.3.5. Alternate site binding of S35 correlates with its activities

To elucidate the effect of S35 binding to the alternate ligand-binding site on PPARγ transactivation, I performed a luciferase reporter gene assay to measure the agonistic activity in PPARγ-mediated transcription in cell. Rosiglitazone and S35 dispalyed concentration-dependent increases on PPARγ transactivation, consistent with previous reports (Koh et al., 2014). To further evaluate whether alternate site ligand binding can affect PPARγ transactivation, I conducted a reporter assay by pretreating cells with GW9662 before administering cells with ligand. GW9662 is a synthetic irreversible PPARγ antagonist that covalently binds to Cys285 (Cys285 in PPARγ1; Cys313 in PPARγ2) on H3 (Leesnitzer et al., 2002). This covalent antagonist GW9662 completely blocks the ligand engagement at the canonical binding pocket while not fully inhibiting alternate site binding of PPARγ ligands (Hughes et al., 2014). Based on the superposition of GW9662 (3B0R) onto the S35-bound structure, S35 exhibits no steric clash with GW9662 (Figure 1-13). Compared to rosiglitazone or S35, GW9662 does not affect the agonistic activity in PPARγ-mediated transcription (Nakano et al., 2006). As shown in Figure 1-14A, coadministration of GW9662 did not affect the action of S35 on PPARγ transactivation, but rather caused a right-shift in the efficacy of S35. Also as previous report

(Hughes et al., 2014), GW9662 blocks the action of rosiglitazone at concentration up to ~2.5 μM, whereas higher rosiglitazone concentrations have the agonistic activity on PPARγ transactivation (Figure 1-14A).

I next performed *in vitro* Cdk5 assay to determine whether S35 binding to the alternate binding site can affect the Cdk5-mediated phosphorylation at Ser273 of PPARγ. GW9662 does not inhibit Cdk5-mediated phosphorylation of PPARγ at 10 μM *in vitro*. In the absence of GW9662 both rosiglitazone and S35 effectively blocked the Cdk5-mediated phosphorylation of PPARγ *in vitro*. However, coadministration of GW9662 completely blocked the inhibitory effect of rosiglitazone on PPARγ phosphorylation, but does not affect the inhibition of PPARγ phosphorylation by S35 (Figure 1-14B). As previous reports, neither Rosiglitazone nor S35 blocked Cdk5-mediated phosphorylation of the Rb protein, a known substrate of Cdk5. This indicated that rosiglitazone and S35 do not affect the fundamental kinase function of Cdk5 but block the phosphorylation of PPARγ selectively and directly (Figure 1-14C).

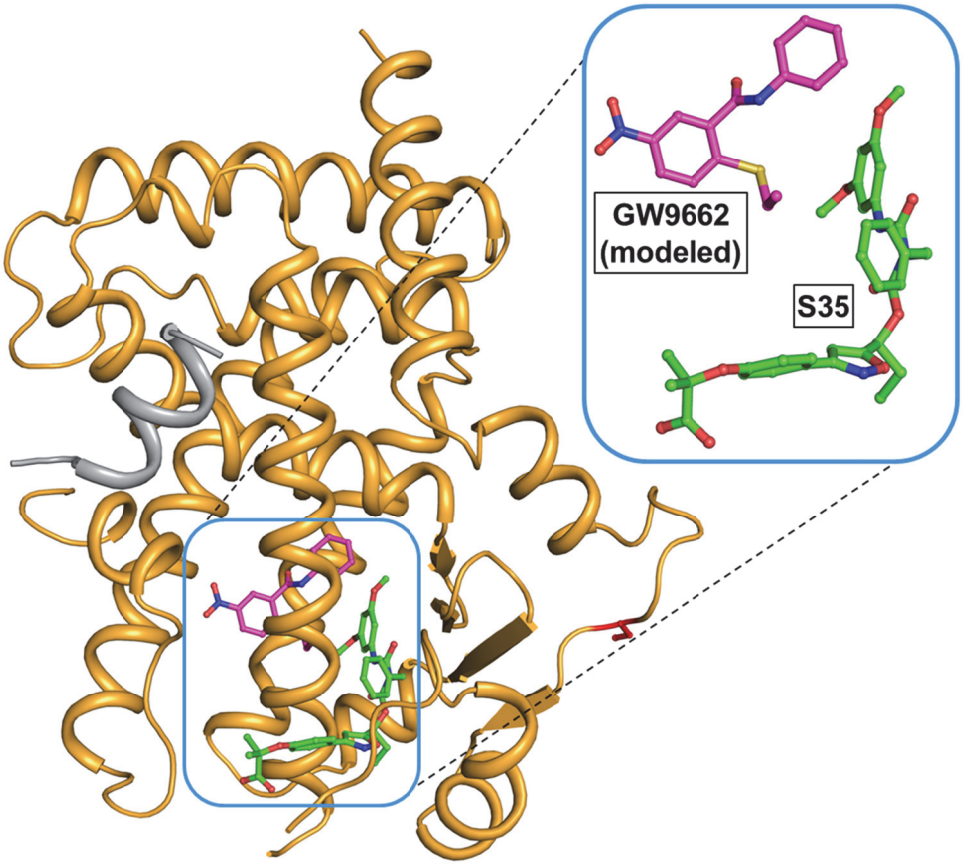

Figure 1-13. Modeling of GW9662 into the S35-bound structure.

The antagonist GW9662-bound structure of PPARγ LBD (magenta, PDB ID: 3B0R) was superimposed onto the S35-bound structure (green). Close-up view on the right demonstrates that no steric clash is expected between S35 and the modeled antagonist GW9662.

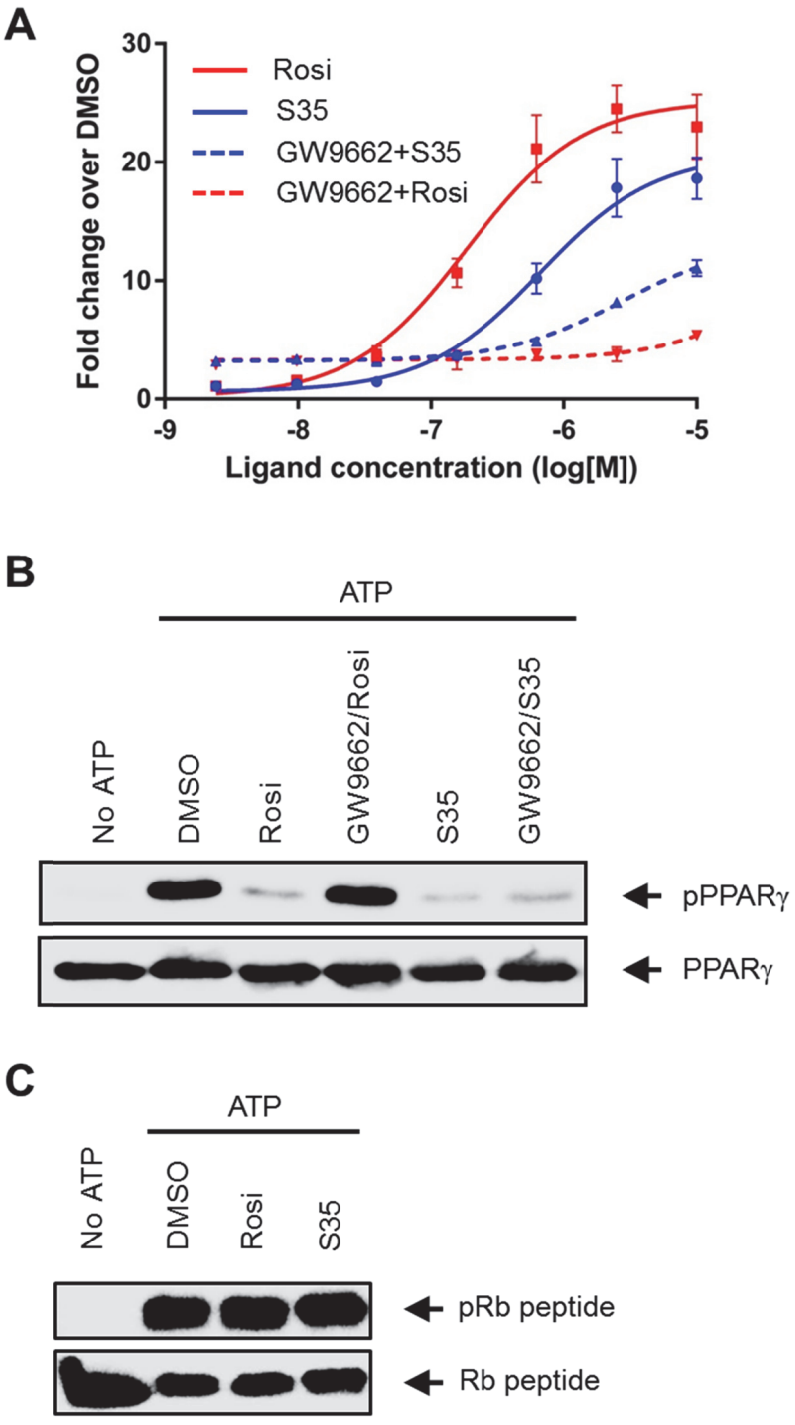
A
Fold change over DMSO
30
20
10
0
-9
-8
-7
-6
-5
Ligand concentration (log[M])
Rosi
S35
GW9662+S35
GW9662+Rosi
B
ATP
No ATP
DMSO
Rosi
GW9662/Rosi
S35
GW9662/S35
pPPARγ
PPARγ
C
ATP
No ATP
DMSO
Rosi
S35
pRb peptide
Rb peptide

Figure 1-14. The effect of S35 binding to the alternate binding site.

(A) Luciferase reporter assay showing the concentration-dependent effects of S35 and rosiglitazone on PPARγ transactivation without GW9662 pretreatment and with GW9662 pretreatment, performed in triplicate and fit to a sigmoidal dose response curve. Error bars represent the standard deviation around the mean value (n = 3). Rosi, rosiglitazone. (B) *In vitro* Cdk5 assay on PPARγ treated by rosiglitazone or S35 with or without GW9662. pPPARγ, phosphorylated PPARγ; Rosi, rosiglitazone. (C) *In vitro* Cdk5 assay on Rb-peptide upon treatment with rosiglitazone or S35. pRb-peptide, phosphorylated Rb-peptide; Rosi, rosiglitazone.

1.4. Discussion

The canonical ligand-binding pocket (LBP) of PPARγ is a Y-shaped hydrophobic cavity with a volume of around 1,200-1,450 $Å^3$. This is much larger than those of most other nuclear receptors. Almost the whole ligands of the PPARγ, which were reported so far, are included in this Y-shaped pocket and affect on the PPARγ activation. Recent NMR study reported that the PPARγ LBD has the alternate ligand-binding site that encompasses an area not thought of as part of the Y-shaped pocket of PPARγ (Hughes et al., 2014). This work is a unique study to identify the alternate ligand-binding site of the PPARγ LBD through the crystal structure. The LBP of the PPARγ LBD from the structure of S35 complex is a large cavity with a volume around 1,560 $Å^3$ and the volume of the alternate ligand-binding site is approximately 200 $Å^3$. The alternate ligand-binding site region is surrounded by helix 3 and the Ω loop between helices 2' and 3. S35 occupies this alternate ligand-binding site and and shows no direct hydrogen bond interactions with the AF2 helix. I observed that S35 induces concentration-dependent increases on PPARγ transactivation with or without coadministered covalent antagonist GW9662 by luciferase reporter assay. GW9662 completely blocks the ligand engagement at the canonical binding

pocket while not fully inhibiting alternate site binding of PPARγ ligands. Furthermore, superposition analysis between S35 and GW9662 shows that GW9662 exhibited no steric clash with S35; thus, S35 and GW9662 can be accommodated simultaneously in the LBP of PPARγ. These results demonstrate that S35 certainly occupies the alternate ligand-binding site and alternate site ligand binding of S35 can affect on the PPARγ transactivation. Recently, the indirect mechanism for the PPARγ agonism through the stabilization induced by alternate site binding was suggested (Bruning et al., 2007; Hughes et al., 2014). The structural data in this study shows that alternate site binding of S35 stabilize helix3 and the Ω loop. Through the indirect mechanism, S35 likely affect on the PPARγ transactivation. However, a different explanation was suggested by observation of the simultaneous binding of a long-chain fatty acid in the S35-bound PPARγ LBP. My data and recent studies have revealed that the canonical LBP of PPARγ can accommodate a multitude of endogenous and synthetic ligands and also simultaneously more than one PPARγ ligand (Waku et al., 2010; Itoh et al., 2008; Puhl et al., 2012). In other word, a endogenous ligand can bind and functionally activate the PPARγ LBD when the alternate site is occupied by a synthetic ligand. This could be another mechanism of the PPARγ agonism by the partial agonists. In contrast, R35 bind to the

canonical LBP that directly stabilize the AF-2 helix through the formation of hydrogen bond network with residues, including Ser289, His323, His449 and Tyr473. Also, the molecular volume of R35 is greater than that of Rosiglitazone, hence R35 has more hydrophobic interaction with the PPARγ LBD than Rosiglitazone. For these strong interaction, R35 likely elicits more robust the agonist activity of the PPARγ than Rosiglitazone (Koh et al., 2014)

Synthetic PPARγ ligands exert PPARγ-driven anti-diabetic action by blocking the phosphorylation of PPARγ at Ser273 by Cdk5 that is a distinct mechanism from the PPARγ transcriptional activity (Choi et al., 2010). The phosphorylation of PPARγ does not change its adipogenic activity but leads to dysregulation of a specific set of genes whose expression is changed in obesity, including lowered expression of the insulin-sensitizing adipokine, adiponectin (Choi et al., 2010). The Cdk5-mediated phosphorylation of PPARγ is blocked by anti-diabetic PPARγ full and partial agonists (Choi et al., 2010). SR1664 is a compound that can block PPARγ phosphorylation at Ser273 and exert potent anti-diabetic activity without activation of classical PPARγ transcriptional agonism (Choi et al., 2011). These reports lead us to expect the development of novel and safer PPARγ-based antidiabetic drugs. However, the lack of understanding of how PPARγ activation by synthetic ligands correlates with the anti-diabetic effect impedes the development of

such synthetic ligands. An activator known as p25, a truncated form of the unstable coactivator p35, hyperactivates Cdk5 in the cellular nucleus (Shukla et al., 2013). Recently, a docking study reports a model for the PPARγ-Cdk5/p25 complex and the molecular interactions between Cdk5 and PPARγ. This docking data suggests that an open conformation of the Ω loop enables the interaction between PPARγ Ω loop and Cdk5/p25 and thus the phosphorylation of PPARγ at Ser273 by Cdk5 occurs. But a closed configuration of the Ω loop induced by ligand binding to PPARγ LBP may prevent the PPARγ-Cdk5/p25 binding mode (Mottin et al., 2015). The structural data in this study also show that binding of either S35 or R35 in the PPARγ LBP induces the closed conformation of the Ω loop, although R35 is not as efficient as S35. These results suggest that alternate site binding of PPARγ could directly affect phosphorylation inhibition through the preventing of Cdk5 binding to PPARγ.

1.5. References

Amano, Y., Yamaguchi, T., Ohno, K., Niimi, T., Orita, M., Sakashita, H., and Takeuchi, M. (2012). Structural basis for telmisartan-mediated partial activation of PPAR gamma. Hypertens. Res. **35**, 715–719.

Ambrosio, A. L., Dias, S. M., Polikarpov, I., Zurier, R. B., Burstein, S. H., and Garratt, R. C. (2007). Ajulemic acid, a synthetic nonpsychoactive cannabinoid acid, bound to the ligand binding domain of the human peroxisome proliferator-activated receptor gamma. J. Biol. Chem. **282**, 18625–18633.

Bensinger, S. J., and Tontonoz, P. (2008). Integration of metabolism and inflammation by lipid-activated nuclear receptors. Nature **454**, 470–477.

Berger, J. and Moller, D. E. (2002). The mechanisms of action of PPARs. Annu. Rev. Med. **53**, 409–435.

Bruning, J. B., Chalmers, M. J., Prasad, S., Busby, S. A., Kamenecka, T. M., He, Y., Nettles, K. W., and Griffin, P. R. (2007). Partial agonists activate PPARgamma using a helix 12 independent mechanism. Structure **15**, 1258–1271.

Brünger, A. T. (1992). The free R-value: a novel statistical quantity for assessing the accuracy of crystal structures. Nature **355**, 472–474.

Chen, V. B., Arendall, W. B., 3rd, Headd, J. J., Keedy, D. A., Immormino, R. M., Kapral, G. J., Murray, L. W., Richardson, J. S., and Richardson, D. C. (2010) MolProbity: all-atom structure validation for macromolecular crystallography. Acta Crystallogr. sect. D Biol. Crystallogr. **66**, 12–21.

Choi, J. H., Banks, A. S., Estall, J. L., Kajimura, S., Boström, P., Laznik, D., Ruas, J. L., Chalmers, M. J., Kamenecka, T. M., Blüher, M., Griffin, P. R., and Spiegelman, B. M. (2010). Anti-diabetic drugs inhibit obesity-linked phosphorylation of PPARgamma by Cdk5. Nature **466**, 451–456.

Choi, J. H., Banks, A. S., Kamenecka, T. M., Busby, S. A., Chalmers, M. J., Kumar, N., Kuruvilla, D. S., Shin, Y., He, Y., Bruning, J. B., Marciano, D. P., Cameron, M. D., Laznik, D., Jurczak, M. J., Schürer, S. C., Vidović, D., Shulman, G. I., Spiegelman, B. M., and Griffin, P. R. (2011). Antidiabetic actions of a non-agonist PPARγ ligand blocking Cdk5-mediated phosphorylation. Nature **477**, 477–481.

Choi, S. S., Kim, E. S., Koh, M., Lee, S. J., Lim, D., Yang, Y. R., Jang, H. J., Seo, K. A., Min, S. H., Lee, I. H., Park, S. B., Suh, P. G., and Choi, J. H. (2014). A novel non-agonist peroxisome proliferator-activated receptor

γ (PPARγ) ligand UHC1 blocks PPARγ phosphorylation by cyclin-dependent kinase 5 (CDK5) and improves insulin sensitivity. J. Biol. Chem. **289**, 26618–26629.

Emsley, P., Lohkamp, B., Scott, W. G., and Cowtan, K. (2010). Features and development of Coot. Acta Crystallogr. sect. D Biol. Crystallogr. **66**, 486–501.

Gallastegui, N., Mackinnon, J. A., Fletterick, R. J., and Estébanez-Perpiñáemail, E. (2015). Advances in our structural understanding of orphan nuclear receptors. Trends Biochem. Sci. **40**, 25–35.

Gampe, R. T., Jr., Montana, V. G., Lambert, M. H., Miller, A. B., Bledsoe, R. K., Milburn, M. V., Kliewer, S. A., Willson, T. M., and Xu, H. E. (2000). Asymmetry in the PPARγ/RXRα crystal structure reveals the molecular basis of heterodimerization among nuclear receptors. Mol. Cell **5**, 545–555.

Hu, X., Li, Y., and Lazar, M. A. (2001). Determinants of CoRNR-dependent repression complex assembly on nuclear hormone receptors. Mol. Cell. Biol. **21**, 1747–1758.

Hughes, T. S., Giri, P. K., de Vera, I. M., Marciano, D. P., Kuruvilla, D. S., Shin, Y., Blayo, A. L., Kamenecka, T. M., Burris, T. P., Griffin, P. R.,

and Kojetin, D. J. (2014). An alternate binding site for PPARγ ligands. Nat. Commun. **5**, Article number 3571.

Itoh, T., Fairall, L., Amin, K., Inaba, Y., Szanto, A., Balint, B. L., Nagy, L., Yamamoto, K., and Schwabe, J. W. (2008). Structural basis for the activation of PPARgamma by oxidized fatty acids. Nat. Struct. Mol. Biol. **15**, 924–931.

Jay, M. A., and Ren, J. (2007). Peroxisome proliferator-activated receptor (PPAR) in metabolic syndrome and type 2 diabetes mellitus. Curr. Diabetes Rev. **3**, 33–39.

Kallenberger, B. C., Love, J. D., Chatterjee, V. K., and Schwabe, J. W. (2003). A dynamic mechanism of nuclear receptor activation and its perturbation in a human disease. Nat. Struct. Biol. **10**, 136–140.

Koh, M., Park, J., Koo, J. Y., Lim, D., Cha, M. Y., Jo, A., Choi, J. H., and Park, S. B. (2014). Phenotypic screening to identify small-molecule enhancers for glucose uptake: target identification and rational optimization of their efficacy. Angew. Chem. Int. Ed. Engl. **53**, 5102–5106.

Leesnitzer, L. M., Parks, D. J., Bledsoe, R. K., Cobb, J. E., Collins, J. L., Consler, T. G., Davis, R. G., Hull-Ryde, E. A., Lenhard, J. M., Patel, L., Plunket, K. D., Shenk, J. L., Stimmel, J. B., Therapontos, C., Willson, T.

M., and Blanchard, S. G. (2002). Functional consequences of cysteine modification in the ligand binding sites of peroxisome proliferator activated receptors by GW9662. Biochemistry **41**, 6640–6650.

Lehrke, M. and Lazar, M. A. (2005). The many faces of PPARγ. Cell **123**, 993–999.

Lewis, S. N., Bassaganya-Riera, J., and Bevan, D. R. (2010). Virtual screening as a technique for PPAR modulator discovery. PPAR Res. **2010**, Article ID 861238.

Loiodice, F. and Pochetti, G. (2011). Structural insight into the crucial role of ligand chirality in the activation of PPARs by crystallographic methods. Curr. Top. Med. Chem. **11**, 819–839.

Luconi, M., Cantini, G., and Serio, M. (2010). Peroxisome proliferator-activated receptor gamma (PPARgamma): Is the genomic activity the only answer? Steroids **75**, 585–594.

Malapaka, R. R., Khoo, S., Zhang, J., Choi, J. H., Zhou, X. E., Xu, Y., Gong, Y., Li, J., Yong, E. L., Chalmers, M. J., Chang, L., Resau, J. H., Griffin, P. R., Chen, Y. E., and Xu, H. E. (2012). Identification and mechanism of 10-carbon fatty acid as modulating ligand of peroxisome proliferator-activated receptors. J. Biol. Chem. **287**, 183–195.

Mottin, M., Souza, P. C., and Skaf, M. S. (2015). Molecular recognition of PPARγ by kinase Cdk5/p25: Insights from a combination of protein-protein docking and adaptive biasing force simulations. J. Phys. Chem. B **119**, 8330−8339.

Murshudov, G. N., Vagin, A. A., and Dodson, E. J. (1997). Refinement of macromolecular structures by the maximum-likelihood method. Acta Crystallogr. sect. D Biol. Crystallogr. **53**, 240–255.

Nakano, R., Kurosaki, E., Yoshida, S., Yokono, M., Shimaya, A., Maruyama, T., and Shibasaki, M. (2006). Antagonism of peroxisome proliferator-activated receptor gamma prevents high-fat diet-induced obesity in vivo. Biochem. Pharmacol. **72**, 42–52.

Nolte, R. T., Wisely, G. B., Westin, S., Cobb, J. E., Lambert, M. H., Kurokawa, R., Rosenfeld, M. G., Willson, T. M., Glass, C. K., and Milburn, M. V. (1998). Ligand binding and co-activator assembly of the peroxisome proliferator-activated receptor-gamma. Nature **395**, 137–143.

Otwinowski, Z. & Minor, W. (1997). Processing of X-ray diffraction data collected in oscillation mode. Methods Enzymol. **276**, 307–326.

Puhl, A. C., Bernardes, A., Silveira, R. L., Yuan, J., Campos, J. L., Saidemberg, D. M., Palma, M. S., Cvoro, A., Ayers, S. D., Webb, P.,

Reinach, P. S., Skaf, M. S., and Polikarpov, I. (2012). Mode of peroxisome proliferator-activated receptor γ activation by luteolin. Mol. Pharmacol. **81**, 788–799.

Ricote, M., Huang, J., Fajas, L., Li, A., Welch, J., Najib, J., Witztum, J. L., Auwerx, J., Palinski, W., Glass, C. K. (1998). Expression of the peroxisome proliferator-activated receptor γ (PPARγ) in human atherosclerosis and regulation in macrophages by colony stimulating factors and oxidized low density lipoprotein. Proc. Natl. Acad. Sci. USA **95**, 7614–7619.

Shukla, V., Zheng, Y. L., Mishra, S. K., Amin, N. D., Steiner, J., Grant, P., Kesavapany, S., and Pant, H. C. (2013). A truncated peptide from p35, a Cdk5 activator, prevents Alzheimer's disease phenotypes in model mice. FASEB J. **27**, 174−186.

Subramani, P. A., Reddy, M. C., and Narala, V. R. (2013). The need for physiologically relevant peroxisome proliferator-activated receptor-gamma (PPAR-γ) ligands. Endocr. Metab. Immune Disord. Drug Targets **13**, 175–183.

Sugii, S. and Evans, R. M. (2011). Epigenetic codes of PPAR gamma in metabolic disease. FEBS Lett. **585**, 2121–2128.

Tontonoz, P., Hu, E., Graves, R. A., Budavari, A. I., and Spiegelman, B. M. (1994). mPPARγ2: tissue-specific regulator of an adipocyte enhancer. Genes Dev. **8**, 1224–1234.

Tsukahara, T., Tsukahara, R., Yasuda, S., Makarova, N., Valentine, W. J., Allison, P., Yuan, H., Baker, D. L., Li, Z., Bittman, R., Parrill, A., and Tigyi, G. (2006). Different residues mediate recognition of 1-O-oleyllysophosphatidic acid and rosiglitazone in the ligand binding domain of peroxisome proliferator-activated receptor γ. J. Biol. Chem. **281**, 3398–3407.

Vagin, A., and Teplyakov, A. (2010) Molecular replacement with MOLREP. Acta Crystallogr. sect. D Biol. Crystallogr. **66**, 22–25.

Waku, T., Shiraki, T., Oyama, T., Maebara, K., Nakamori, R., and Morikawa, K. (2010). The nuclear receptor PPARγ individually responds to serotonin- and fatty acid-metabolites. EMBO J. **29**, 3395–3407.

Walczak, R. and Tontonoz, P. (2002). PPARadigms and PPARadoxes: expanding roles for PPARγ in the control of lipid metabolism. J. Lipid Res. **43**, 177–186.

Xu, H. E., and Li, Y. (2008). Ligand-dependent and -independent regulation of PPAR gamma and orphan nuclear receptors. Sci. Signal. **1**, pe52.

Zhu, Y., Qi, C., Korenberg, J. R., Chen, X. N., Noya, D., Rao, M. S., and Reddy, J. K. (1995). Structural organization of mouse peroxisome proliferator-activated receptor gamma (mPPAR gamma) gene: alternative promoter use and different splicing yield two mPPAR gamma isoforms. Proc. Natl. Acad. Sci. USA **92**, 7921–7925.

Chapter 2

Crystal structure of the TNF-α inducing protein (Tipα) from *Helicobacter pylori*: Insights into its DNA binding activity

[This chapter was published in J. Mol. Biol. (2009) 392, 191–197.]

2.1. Introduction

Helicobacter pylori is a helical-shaped, Gram-negative bacterium that lives in the human stomach and duodenum. *H. pylori* infection is one of the highest risk factors for gastroduodenal diseases including gastric cancer (IARC working group, 1994). It has long been known that *H. pylori* infection results in an inflammatory response in the stomach by induction of various cytokines such as tumor necrosis factor-α (TNF-α), interleukin-1, and interleukin-8 (Peek and Blaser, 2002). TNF-α is one of the essential cytokines for tumor promotion and thus a gene product of *H. pylori* that induces TNF-α is believed to play a significant role in gastric cancer development in humans (Moore et al., 1999; Suganuma et al., 1999;

Suganuma et al., 2008). The *HP0596* gene product of *H. pylori* strain 26695 was identified as the TNF-α inducing protein (Tipα) (Suganuma et al., 2005). The *HP0596* gene encodes a protein of 192 amino acid residues with a signal peptide cleavage site between residues 20 and 21 (Suganuma et al., 2005). The *HP0596* gene product has no sequence similarity to other virulence factors of *H. pylori* such as vacuolating cytotoxin and cytotoxin-associated antigen (CagA). A cell fractionation experiment indicates that Tipα is anchored to the inner membrane of *H. pylori* (Godlewska et al., 2008; Yoshida et al., 1999). Tipα is secreted as a homodimer of the mature polypeptide (residues 21–192), which contains the only two cysteines (Cys25 and Cys27) of Tipα in the N-terminus for the possible formation of inter-chain disulfide bonds (Suganuma et al., 2005) (Figure 2-1). Clinical isolates of *H. pylori* obtained from gastric cancer patients secreted the Tipα protein significantly more than did those from gastritis patients, suggesting that *H. pylori* Tipα is an essential factor in inflammation and carcinogenesis in the stomach (Suganuma et al., 2008) (Figure 2-2). Secreted Tipα binds to mouse gastric epithelial cells MGT-40, presumably through the action of an uncharacterized receptor (Suganuma et al., 2005; Suganuma et al., 2008), and enters those cells, resulting in the expression of TNF-α and various chemokine genes (Suganuma et al., 2005; Suganuma et al., 2008; Kuzuhara

et al., 2007a). A deletion mutant of Tipα (del-Tipα; residues 28–192 fused with an N-terminal His tag), which lacks six residues 21–27 containing Cys25 and Cys27, neither bound nor entered the gastric cells, suggesting that a dimer formation of Tipα with one or two disulfide bonds is required for both specific binding to gastric cells and induction of TNF-α gene expression (Suganuma et al., 2008). A confocal laser scanning microscope analysis revealed that a significant amount of *H. pylori* Tipα is localized in the nucleus of the gastric cancer cells (Suganuma et al., 2008). Tipα was shown to activate NF-κB in mouse gastric epithelial cells MGT-40 and to induce *in vitro* transformation of v-H-*ras* transfected BALB/3T3 (Bhas 42) cells (Suganuma et al., 2005; Suganuma et al., 2006). The DNA-binding activity of Tipα secreted from *H. pylori* was also demonstrated by the pull-down and surface plasmon resonance assays (Kuzuhara et al., 2007b). The recombinant Tipα (residues 21–192) also bound to TNF-α promoter sequences dose-dependently and its DNA-binding affinity was much higher than del-Tipα (residues 28–192), which lacks the two cysteine residues Cys25 and Cys27 (Kuzuhara et al., 2007b).

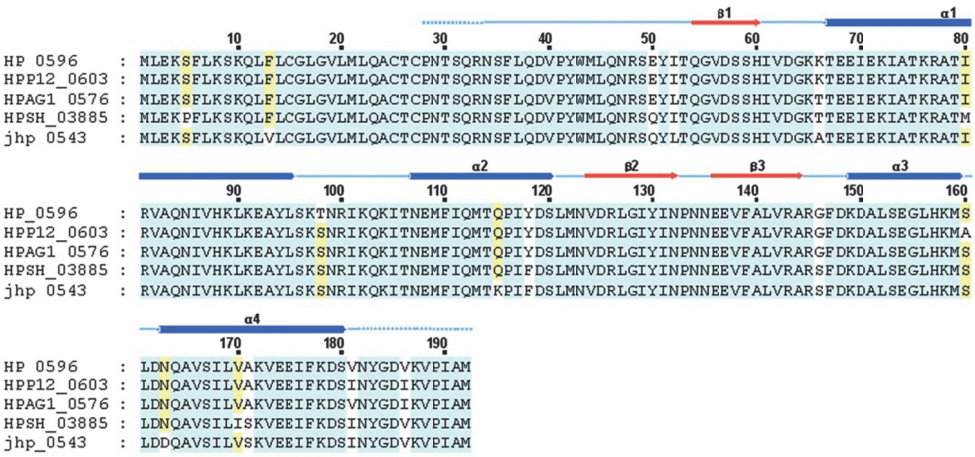

Figure 2-1. Sequence alignment of *H. pylori* Tipα and its homologs, and secondary structure assignment of HP0596.

Strictly conserved residues are highlighted by the cyan background. The dotted lines above the sequence denote disordered residues. HP_0596: Tipα from *H. pylori* (strain 26695), EXPASY accession number O25318. HPP12_0603: Tipα from *H. pylori* (strain P12), B6JLH8. HPAG1_0576: Tipα from *H. pylori* (strain HPAG1), Q1CTS9. HPSH_03885: Tipα from *H. pylori* (strain Shi470), B2UTN0. jhp_0543: Tipα from *H. pylori* (strain J99), Q9ZLN5.

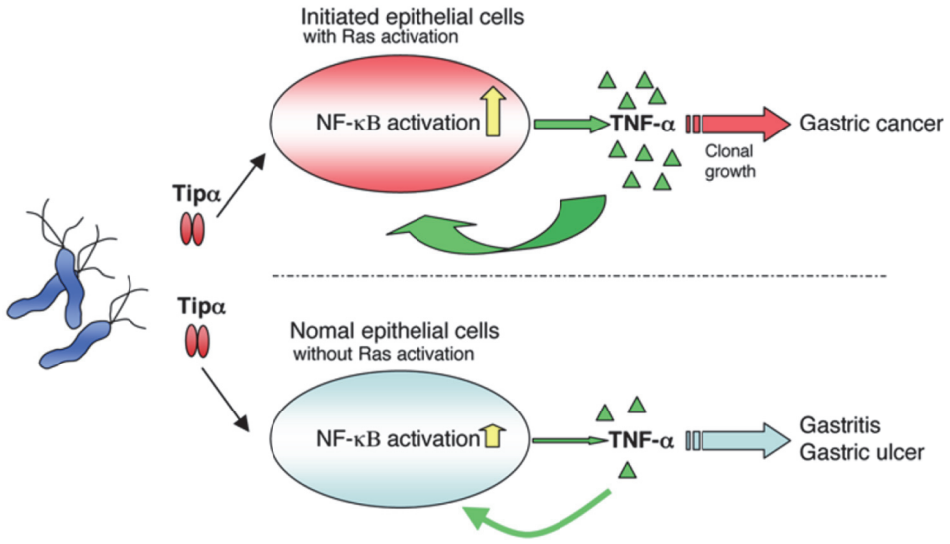

Figure 2-2. Schematic illustration for the carcinogenic role of *H. pylori* Tipα. [Suganuma et al. (2006) *J. Biochem. Mol. Biol.* **39(1)**, 1-8]

Very weak sequence homology between *H. pylori* Tipα and penicillin-binding proteins from Gram-positive bacteria was detected, but the functional significance of this distant homology is unclear (Kuzuhara et al., 2005). Prediction of the three-dimensional model of Tipα by sequence structure threading suggested that it may adopt a four-α-helical-bundle fold (Godlewska et al., 2008). However, a detailed three-dimensional structure of Tipα is required to provide a structural basis for better understanding of DNA-binding by Tipα and thus the carcinogenic mechanism of Tipα. In this study, we have determined the crystal structure of Tipα from *H. pylori* by the multiwavelength anomalous diffraction (MAD) method of X-ray crystallography. It reveals that *H. pylori* Tipα adopts a new fold for a DNA-binding protein family and that the N-terminally truncated Tipα (residues 28–192) exists as a dimer in the crystal. Site-directed mutagenesis suggests that a positively charged surface patch formed across the two monomers of the Tipα dimer by the loop between helices α1 and α2 may be important in DNA binding.

2.2. Material and methods

2.2.1. Protein expression and purification

The *H. pylori* Tipα gene (*HP0596*) encoding the N-terminally truncated form (residues 28–192) was PCR-amplified and cloned into the expression vector pET-28b(+) (Novagen). This construct of the recombinant protein contains a hexa-histidine-containing 21-residue extra sequence (MGSSHHHHHH SSGLVPRGSH M) in front of the starting residue Pro28. It is identical to del-Tipα (Suganuma et al., 2005; Kuzuhara et al., 2007b). The recombinant protein substituted with SeMet was overexpressed in *E. coli* Rosetta2(DE3)pLysS cells using M9 culture medium supplemented with SeMet. Protein expression was induced by 0.5 mM isopropyl 1-thio-β-D-galactopyranoside and the cells were incubated for an additional 24 h at 30°C after growth to the mid-long phase at 37°C. The cells were lysed by sonication in a lysis buffer (50 mM Tris-HCl at pH 7.9, 500 mM NaCl, and 10% (v/v) glycerol) containing 50 mM imidazole. The crude lysate was centrifuged at ~36,000 g for 60 min. The supernatant was applied to an affinity chromatography column of HiTrap Chelating HP (GE Healthcare). The protein was eluted with the lysis buffer containing 500 mM imidazole

and the eluted sample was diluted tenfold with buffer A (20 mM sodium phosphate at pH 6.0). The diluted sample was applied to a Hitrap SP HP column (5 ml) (GE Healthcare), previously equilibrated with buffer A. Upon eluting with a gradient of NaCl in the same buffer, Tipα was eluted at 360–480 mM NaCl concentration. The next step was gel filtration on a HiLoad XK-16 Superdex 200 prep-grade column (GE Healthcare), previously equilibrated with 20 mM citric acid at pH 4.0 and 200 mM NaCl. The eluted protein was concentrated to 11 mg ml^{-1} for crystallization using an Amicon Ultra-15 centrifugal filter unit (Millipore). Dynamic light scattering experiments were performed on a DynaPro-801 instrument (Wyatt) at ~1 mg ml^{-1} protein dissolved in the same buffer used in gel filtration on the Superdex 200 column.

2.2.2. Mutagenesis and electrophoretic mobility shift assay

The mature Tipα (residues 21–192), containing Cys25 and Cys27, was mutated using the QuikChange site-directed mutagenesis kit (Stratagene) and the mutations were confirmed by DNA sequencing. The K102A/K104A double mutant was expressed and purified under the conditions identical to those for the wild-type. The double mutant showed a similar elution profile as the wild-type upon gel filtration. SDS-PAGE analysis indicated that the double mutant as well as the wild-type Tipα migrated as a dimer in the absence of β-mercaptoethanol but was present as a monomer in the presence of β-mercaptoethanol. We mixed 1.5 or 3.0 μl of Tipα (3.7 μg μl^{-1}) and 3.0 μl of a linear dsDNA with 545 base pairs (140 ng μl^{-1}), corresponding to the molar ratio of 10:1 or 20:1 for Tipα dimer to dsDNA. The reaction mixtures were incubated for 20 min at room temperature. Binding of Tipα to dsDNA was analyzed by 0.5 %(*w/v*) agarose gel electrophoresis in 1×TAE buffer (45 mM Tris-acetate at pH 8.3, 1 mM EDTA). DNA bands were visualized by ethidium bromide staining.

2.2.3. Crystallization and data collection

Crystals were grown by hanging-drop vapor diffusion method by mixing equal volumes of the protein solution and the reservoir solution (100 mM Tris-HCl at pH 7.0, 200 mM calcium acetate, and 20% (w/v) PEG 3000) (Figure 2-3). They were transferred to a cryoprotectant solution which contained 15% (v/v) glycerol in the reservoir solution. Two sets (SeMet I and SeMet II) of MAD data were collected at 100 K on an ADSC Quantum 315 detector at the BL-5A experimental station of Photon Factory (PF), Japan and on an ADSC Quantum 210 CCD detector (Area Detector Systems Corporation, Poway, California) at the BL-4A experimental station of Pohang Light Source (PLS), Korea, respectively. The raw data were processed and scaled using the program suit HKL2000 (Otwinowski and Minor, 1997). The crystals belong to the space group $P2_12_12_1$, with unit cell parameters of a = 53.52 Å, b = 67.11 Å, and c = 91.26 Å for the SeMet II (remote) data (Table 2-1). Two monomers of Tipα are present in the asymmetric unit, giving V_M of 1.93 $Å^3$/Da and a solvent content of 36.4%.

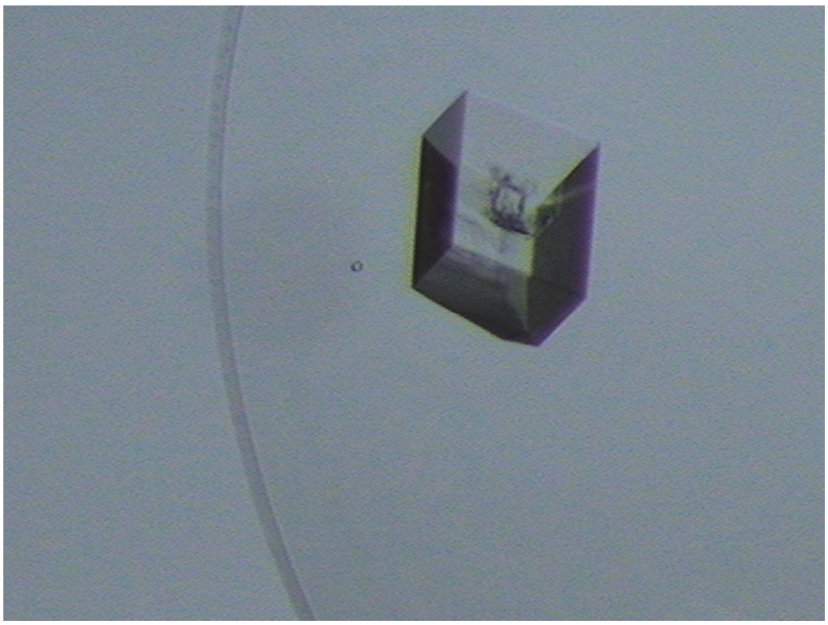

Figure 2-3. A crystal of *H. pylori* Tipα.

Its approximate dimensions of 0.2 mm × 0.2 mm × 0.1 mm.

Table 2-1. Data collection and phasing statistics

Data collection				
Data set	SeMet I (inflection)	SeMet I (peak)	SeMet I (remote)	SeMet II (remote)
X-ray source	PF BL-5A	PF BL-5A	PF BL-5A	PLS BL-4A
X-ray wavelength (Å)	0.97912	0.97885	0.96000	0.96000
Temperature (K)	100	100	100	100
Space group	$P2_12_12_1$	$P2_12_12_1$	$P2_12_12_1$	$P2_12_12_1$
a, *b*, *c* (Å)	52.55, 66.43, 90.55	52.55, 66.47, 90.54	52.58, 66.49, 90.58	53.52, 67.11, 91.26
Resolution range (Å)	50.0–2.70 (2.80–2.70)	50.0–2.70 (2.80–2.70)	50.0–2.70 (2.80–2.70)	30.0–2.40 (2.49–2.40)
Total/unique reflections	116,922 / 9,199	231,055 / 9,137	117,732 / 9,096	214,284 / 13,650
R_{merge}[a] (%)	8.3 (37.4)	9.8 (41.4)	9.0 (36.4)	9.3 (42.2)
Data completeness (%)	99.8 (90.0)	98.7 (89.4)	98.3 (90.3)	100.0 (100.0)
Average $I/\sigma(I)$	56.7 (3.7)	76.7 (4.7)	57.1 (4.0)	42.9 (7.2)
MAD phasing	Figure of merit[b] for MAD phasing: 0.73/0.88 for 20.0–2.70 Å data (before/after density modification)			

Footnote to Table 2-1

Values in parentheses refer to the highest resolution shells [2.80–2.70 Å for the SeMet I MAD data and 2.49–2.40 Å for the SeMet II (remote) data].

[a] $R_{merge} = \Sigma_h \Sigma_i \mid I(h)_i - \langle I(h) \rangle \mid / \Sigma_h \Sigma_i I(h)_i$, where $I(h)_i$ is the intensity of the i-th measurement of reflection h and $\langle I(h) \rangle$ is the mean value of I(h) for all i measurements.

[b] Figure of merit = $\langle \mid \Sigma P(\alpha) \exp(i\alpha) / \Sigma P(\alpha) \mid \rangle$, where α is the phase angle and P(α) is the phase probability distribution.

2.2.4. Structure solution and refinement

Ten of the fourteen expected selenium atoms of the two monomers in each crystallographic asymmetric unit were located with the program SOLVE (Terwilliger and Berendzen, 1999), and the selenium sites were used to calculate and improve the phases with RESOLVE (Terwilliger, 2003). The resulting electron density map was interpreted by the automatic model building program RESOLVE, which generated an initial model that accounted for ~37% of the residues in the polypeptide chain with much of the sequence assigned. Subsequent manual model building was conducted using the program COOT (Emsley and Cowtan, 2004). The model was refined with the program REFMAC (Murshudov et al., 1997), including the bulk solvent correction. Ten percent of the data were randomly set aside as the test data for the calculation of R_{free} (Brünger, 1992). The program PROCHECK was used to assess the stereochemistry and to assign the secondary structure elements (Laskowski et al., 1993). Refinement statistics are presented in Table 2-2.

Table 2-2. Refinement statistics

Refinement	
Data set	SeMet II (remote)
Resolution range (Å)	30.0–2.40
No. of reflections (working/free set)	12,433 / 714
No. of protein non-hydrogen atoms	2,391
No. of water molecules	70
R_{work}/R_{free} [a] (%)	23.3 / 24.1
R.m.s. deviations from ideal geometry	
Bond length (Å)	0.0067
Bond angle (°)	1.15
Average *B*-factor (Å^2)	
Protein	41.1
Water molecules	43.6
Ramachandran plot for non-glycine and non-proline residues[b]	
Most favorable regions (%) (chains A/B)	92.8 / 90.6
Allowed regions (%) (chains A/B)	6.5 / 9.4
Generously allowed regions (%) (chains A/B)	0.7 / 0.0

Footnotes to Table 2-2

[a] $R_{work} = \Sigma \mid |F_{obs}| - |F_{calc}| \mid / \Sigma |F_{obs}|$, where R_{free} is calculated for a randomly chosen 10% of reflections, which were not used for structure refinement, and R_{work} is calculated for the remaining reflections.

[b] Values obtained using PROCHECK.

2.3. Results and discussion

2.3.1. Model quality and structure of Tipα monomer

We have solved the crystal structure of *H. pylori* Tipα (residues 28–192) using selenomethionine (SeMet) MAD data. The model was refined against the SeMet II (remote) data (Table 2-2); it yielded R_{work} and R_{free} values of 23.3% and 24.1% for 30.0–2.40 Å data, respectively. The model contains 296 residues in two monomers of Tipα (residues 34–181 for both chains A and B) and 70 water molecules in the crystallographic asymmetric unit (Table 2-2). The missing residues of Tipα and the N-terminal fusion tag are probably disordered in the crystal and are invisible in the electron density map. An N-terminal loop region (residues 34–36 and 46–51 for chain A; residues 34–35 and 48–51 for chain B), a loop between β1 and α1 (residues 62–63 for chain B), a loop between β2 and α2 (132–136 for chain B), and a C-terminal region (179–181 for chain B) show relatively high *B*-factors (> 60 $Å^2$).

A monomer of Tipα (residues 28–192) consists of four α-helices, three β-strands, and a number of loops. Each monomer is somewhat elongated and curved. It may be loosely divided into two structural domains (“mixed domain” and “helical domain”), with the longest helix α1 being shared between them and providing a platform for building the two structural domains (Figure 2-4). The first domain (“mixed domain”) consists of a central three-stranded antiparallel β-sheet (β1↑-β3↓-β2↑) that covers the N-terminal half of the longest helix α1. A long N-terminal loop covers the other face of central β-sheet. The two β-strands β2 and β3 are inserted between helices α2 and α3. The other domain (“helical domain”) is a four-helix bundle formed of the helices α1 (the C-terminal half), α2, α3, and α4 (Figure 2-5). The hydrophobic core of the bundle is formed by Val82, Leu90, Ile117, Leu152, Leu156, Val169, and Val173. The four-helix bundle is a common structural motif that occurs in many structural contexts and in proteins that are functionally diverse (Kamtekar and Hecht, 1995).

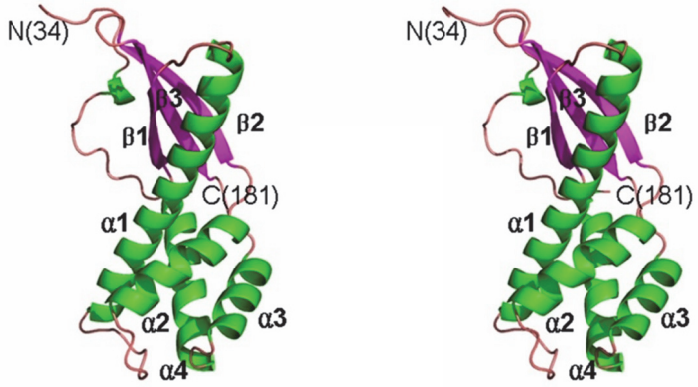

Figure 2-4. Structure of *H. pylori* Tipα monomer.

Stereo ribbon diagram of a monomer.

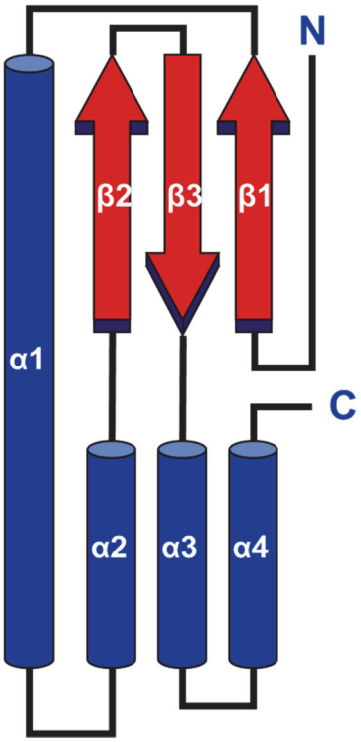

Figure 2-5. Topology diagram of *H. pylori* Tipα monomer.

2.3.2. Structure of Tipα dimer

The crystallographic asymmetric unit contains two monomers (chains A and B) of *H. pylori* Tipα. They show essentially the same conformation. Between chains A and B, the root-mean-square (r.m.s.) deviation is 0.56 Å for 148 Cα atom pairs and a maximum Cα deviation of 3.2 Å occurs at Ser49. The two monomers of Tipα in the asymmetric unit are related by a two-fold non-crystallographic symmetry and they form a tight dimer (Figure 2-6). The dimer formation buries an accessible surface area of 1,560 $Å^2$. There are no other possible dimers in the crystal. Our dynamic light scattering measurement was consistent with the existence of recombinant Tipα as a dimer in the solution.

The Tipα dimer in the asymmetric unit resembles a twisted doughnut (Figure 2-7), with dimensions of 52 Å × 46 Å × 25 Å. Contacts between the monomers are made through two distinct regions. The first is the long N-terminal loop (residues 34–50 and 55–58) and a segment between strands β2 and β3 (residues 130, 132, 135, 137, 139) in the "mixed domain." The second is a segment between helices α1 and α2 (residues 81, 85, 88, 91, 92, 94–99, 104–108, 110) in the "helical domain." The interface area contributed by the "mixed domain" is nearly twice that contributed by the "helical domain." This mode of dimerization results in a small hole of ~8 Å in

diameter (Figure 2-7). If the N-terminal residues absent in our Tipα structure are assumed to be extended and to point toward each other in the bulk solvent, one or both of Cys25 and Cys27 could form one or two inter-chain disulfide bonds. It is likely that the resulting dimer structure of Tipα (residues 21–192) would not significantly deviate from that of del-Tipα (residues 28–192).

Gel electrophoresis showed that the recombinant del-Tipα protein was monomeric without any influence of dithiothreitol (DTT), while the recombinant Tipα was a dimer in the absence of DTT and a monomer with DTT (Suganuma et al., 2005). This discrepancy between our observation of a stable dimer of del-Tipα in the crystal and the reported monomer of del-Tipα could be due to much different protein concentrations used in different experiments. Dimers of Tipα as well as del-Tipα that exist at high protein concentrations may dissociate into monomers at very low protein concentrations, if they are not stabilized by a disulfide bond. Thus, the inter-chain disulfide bond(s) formed by Cys25 and Cys27 may be necessary to prevent dissociation of the secreted Tipα dimer into monomers.

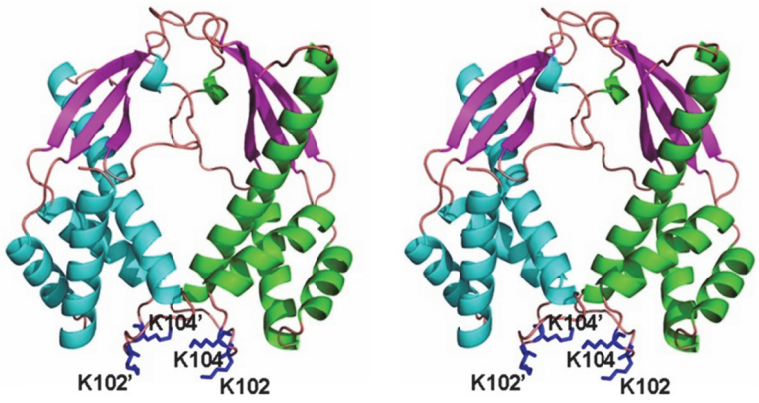

Figure 2-6. Structure of *H. pylori* Tipα dimer.

Stereo ribbon diagram of a dimer. α-Helices are colored in green (chain A) or cyan (chain B). β-Strands, and loops are colored in magenta and pink, respectively. Side chains of mutated residues (Lys102 and Lys104) are shown.

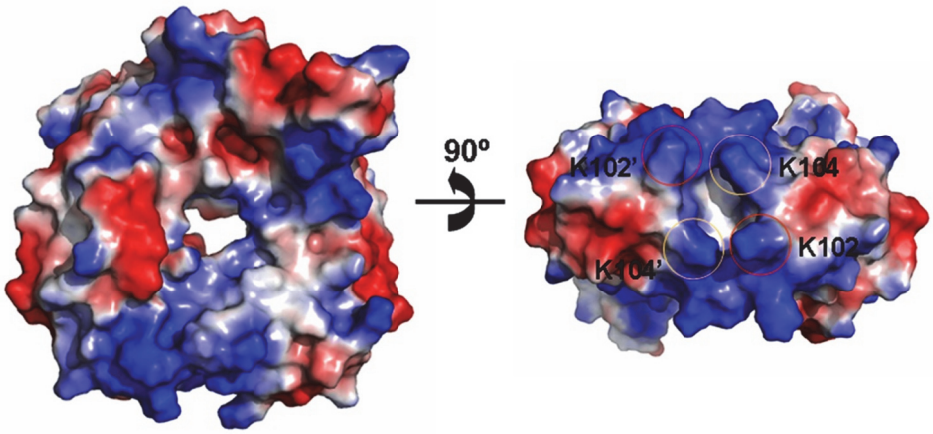

Figure 2-7. Surface electrostatic potential of *H. pylori* Tipα dimer.

The positive electrostatic potential at the molecular surface is colored in blue and the negative potential in red. The structure figures were drawn using the program PyMOL (DeLano, W. L. (2002) *The PyMol Molecular Graphics System.* DeLano Scientific, Palo Alto, CA, USA).

2.3.3. Structural similarity searches

A search for structural homologs of *H. pylori* Tipα monomer in the Protein Data Bank using the DALI server (Holm and Sander, 1996) revealed that there is no highly similar structure. The highest Z-score was only 5.7; it was obtained with the N-terminal domain (NTD) of Nab2 (residues 1–97) (PDB code 2V75) (Grant et al., 2008). The sequence identity between them is only 7% and the r.m.s. deviation is 3.0 Å for 71 Cα atoms in the α1–α2 and α3–α4 regions of the Tipα "helical domain" and the α1–α4 region of Nab2 NTD. The arrangement of four α-helices in the "helical domain" of Tipα is similar to that of the first four α-helices in Nab2 NTD (Grant et al., 2008). Nab2 NTD is largely helical with five α-helices and has no β-strand. Compared with the "helical domain" of Tipα, an extra fifth C-terminal helix α5 lies approximately antiparallel to the N-terminal helix α1 in Nab2 NTD (Figure 2-8). The helical fold of Nab2 NTD is similar to the PWI fold found in several other RNA-binding proteins (Grant et al., 2008). Other PWI fold proteins such as the U4/U6 small nuclear ribonucleoprotein, Prp3 (PDB code 1X4Q) and SRm160-PWI motif (PDB code 1MP1) are also mostly helical (Szymczyna et al., 2003). Nab2 NTD mediates protein-protein interactions and there is no evidence that Nab2 NTD binds to nucleic acids (Grant et al., 2008). In contrast, Srm160-PWI motif binds to double-stranded (ds) and

single-stranded (ss) RNA/DNA (Szymczyna et al., 2003). Furthermore, Nab2 NTD, Prp3, and SRm160-PWI motif are all monomeric. SRm160-PWI motif contains the characteristic Pro-Trp-Ile sequence in helix H1 (Szymczyna et al., 2003), whereas Nab2 NTD and *H. pylori* Tipα lack such a sequence. All of these taken together indicate that the distant structural resemblance between the "helical domain" of Tipα and the PWI fold proteins such as Nab2 NTD is not likely to be functionally relevant. Therefore, our structure of *H. pylori* Tipα appears to represent the first structure of a novel DNA-binding protein family.

The crystal structures of a truncated form of Tipα (TipαN34) in two different crystal forms were reported (Tosi et al., 2009). It has been suggested that crystal form I dimer at pH 4 is likely a crystallization artifact and that TipαN34 dimer observed in crystal from II at pH 8.5 is more likely to be relevant in solution. The latter structure is highly similar to our dimer structure obtained at near neutral pH.

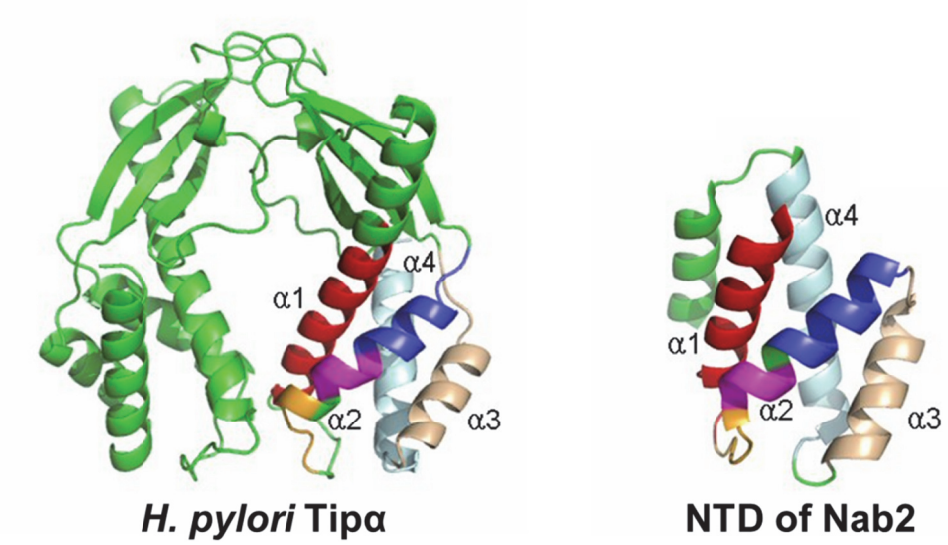

Figure 2-8. Structural comparison of *H. pylori* Tipα with NTD of Nab2.

The structure of the N-terminal Mlp1-binding domain of the *Saccharomyces cerevisiae* mRNA-binding protein, Nab2 (PDB code 2V75), is shown on the right.

2.3.4. Insights into DNA-binding activity

The Tipα dimer is toroidal, with the C-terminal part (residues 85–92) of helix α1 and the loop region (residues 46–52) immediately before strand β1 contributing to form a hole of ~8 Å in diameter (Figure 2-7). Central holes in a number of toroidal proteins involved in DNA metabolism have a diameter of ~20–25 Å to hold ds-DNA (Hingorani and O'Donnel, 2000). In contrast, the central hole of Tipα dimer is too narrow to encircle ds-DNA. The surface electrostatic potential of Tipα dimer suggests that a positively charged surface region at the bottom of Tipα dimer in Figure 2-7, formed across two monomers by the loop between helices α1 and α2 (residues 96–106), could be important in DNA binding. To assess the role of this region in DNA binding, we have mutated two positively charged residues Lys102 and Lys104 into alanine. Electrophoretic mobility shift assay indicated that the dsDNA binding ability of the double mutant (K102A/K104A) was considerably diminished compared to the wild-type Tipα (Figure 2-9). This result supports our proposed DNA binding site.

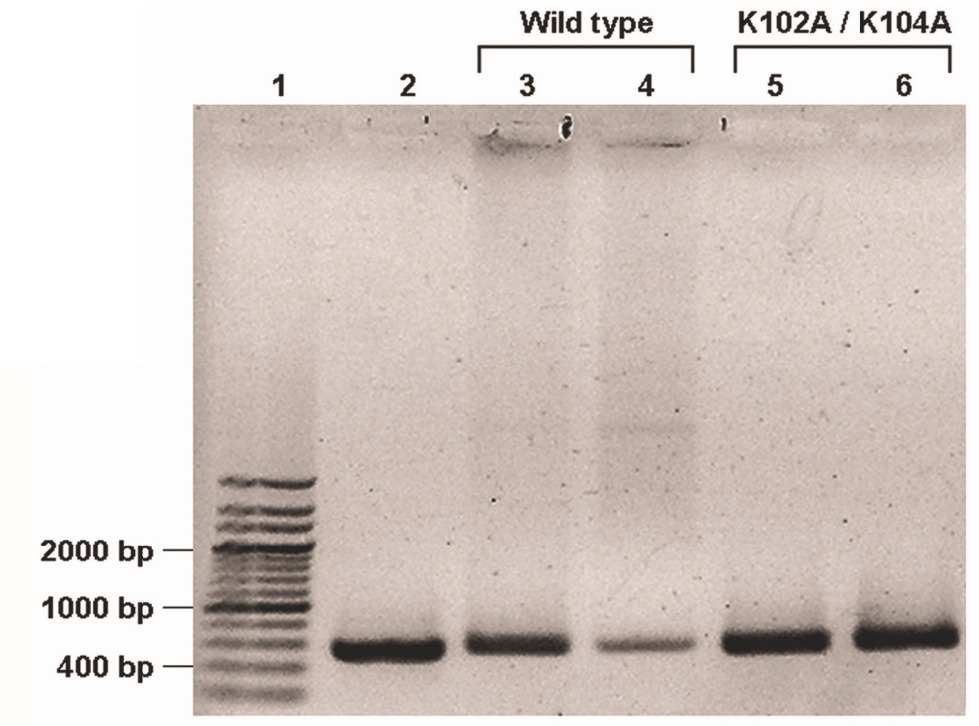

Figure 2-9. Electrophoretic mobility shift assay for dsDNA binding by the mature Tipα (21-192).

Detailed reaction conditions are described in Materials and Methods. Lane 1, 200 bp dsDNA ladder marker; lane 2, linear dsDNA (a 545-base pair PCR product; 420 ng); lane 3, wild-type Tipα (21-192) (5.6 μg); lane 4, wild-type Tipα (11.1 μg); lane 5, K102A/K104A mutant (5.6 μg); lane 6, K102A/K104A mutant (11.1 μg). Binding of the wild-type Tipα to dsDNA resulted in a dose-

dependent decrease of the dsDNA band intensity, whereas the double mutant did not show such a decrease.

2.3.5. Accession number

Atomic coordinates and structure factors of *H. pylori* Tipα have been deposited in the Protein Data Bank (http://www.rcsb.org/pdb) under accession code 3GIO.

2.4. Conclusion

In summary, I have determined the crystal structure of *H. pylori* Tipα (residues 28–192). It exists as a dimer in the crystal and its dimeric structure represents a novel scaffold for DNA-binding. Recently, a small molecule inhibitor of nucleophosmin oligomerization was found to inhibit proliferation of cancer cells (Qi et al., 2008). The structural information reported in this study can provide a starting point for discovering small molecule inhibitors that block homodimerization of *H. pylori* Tipα and thus modulate its biological activity.

2.5. References

Brünger, A. T. (1992). The free R-value: a novel statistical quantity for assessing the accuracy of crystal structures. Nature, **355**, 472–474.

Godlewska, R., Pawlowski, M., Dzwonek, A., Mikula, M., Ostrowski, J., Drela, N. & Jagusztyn-Krynicka, E. K. (2008). Tip-α (hp0596 gene product) is a highly immunogenic Helicobacter pylori protein involved in colonization of mouse gastric mucosa. Curr. Microbiol. **56**, 279–286.

Grant, R. P., Marshall, N. J., Yang, J. C., Fasken, M. B., Kelly, S. M., Harreman, M. T., Neuhaus, D., Corbett, A. H. & Stewart, M. (2008). Structure of the N-terminal Mlp1-binding domain of the Saccharomyces cerevisiae mRNA-binding protein, Nab2. J. Mol. Biol. **376**, 1048–1059.

Hingorani, M. M. & O'Donnell, M. (2000). A tale of toroids in DNA metabolism. Nature Rev. Mol. Cell Biol. **1**, 22–30.

Emsley, P. & Cowtan, K. (2004). Coot: model-building tools for molecular graphics. Acta Crystallogr. sect. D Biol. Crystallogr. **60**, 2126–2132.

Holm, L. & Sander, C. (1995). Dali: a network tool for protein structure comparison. Trends Biochem. Sci. **20**, 478–480.

IARC Working Group on the Evaluation of Carcinogenic Risks to Humans. Infection with *Helicobacter pylori*. (1994). Schistosomes, liver flukes and *Helicobacter pylori*. In IARC monographs on the evaluation of carcinogenic risk to humans (IARC ed.) Vol. 61, pp. 177–240. IARC, Lyon.

Kamtekar, S. & Hecht, M. H. (1995). Protein motifs. 7. The four-helix bundle: what determines a fold? FASEB J. **9**, 1013–1022.

Kuzuhara, T., Suganuma, M., Kurusu, M. & Fujiki, H. (2007a). *Helicobacter pylori*-secreting protein Tipα is a potent inducer of chemokine gene expressions in stomach cancer cells. J. Cancer Res. Clin. Oncol. **133**, 287–296.

Kuzuhara, T., Suganuma, M., Oka, K. & Fujiki, H. (2007b). DNA-binding activity of TNF-α inducing protein from *Helicobacter pylori*. Biochem. Biophys. Res. Commun. **362**, 805–810.

Kuzuhara, T., Suganuma, M., Tsuge, H. & Fujiki, H. (2005). Presence of a motif conserved between *Helicobacter pylori* TNF-α inducing protein (Tipα) and penicillin-binding proteins. Biol. Pharm. Bull. **28**, 2133–2137.

Laskowski, R. A., MacArthur, M. W., Moss, D. S. & Thornton, J. M. (1993). PROCHECK: a program to check the stereochemical quality of protein structures. J. Appl. Crystallogr. **26**, 283–291.

Moore, R. J., Owens, D. M., Stamp, G., Arnott, C., Burke, F., East, N., Holdsworth, H., Turner, L., Rollins, B., Pasparakis, M., Kollias, G. & Balkwill, F. (1999). Mice deficient in tumor necrosis factor-α are resistant to skin carcinogenesis. Nat. Med. **5**, 828–831.

Murshudov, G. N., Vagin, A. A. & Dodson, E. J. (1997). Refinement of macromolecular structures by the maximum-likelihood method. Acta Crystallogr. sect. D Biol. Crystallogr. **53**, 240–255.

Peek, R. M. Jr. & Blaser, M. J. (2002). *Helicobacter pylori* and gastrointestinal tract adenocarcinomas. Nat. Rev. Cancer, **2**, 28–37.

Otwinowski, Z. & Minor, W. (1997). Processing of X-ray diffraction data collected in oscillation mode. Methods Enzymol. **276**, 307–326.

Qi, W., Shakalya, K., Stejskal, A., Goldman, A., Beeck, S., Cooke, L. & Mahadevan, D. (2008). NSC348884, a nucleophosmin inhibitor disrupts oligomer formation and induces apoptosis in human cancer cells. Oncogene **27**, 4210–4220.

Suganuma, M., Okabe, S., Marino, M. W., Sakai, A., Sueoka, E. & Fujiki, H. (1999). Essential role of tumor necrosis factor α (TNF-α) in tumor promotion as revealed by TNF-α-deficient mice. Cancer Res. **59**, 4516–4518.

Suganuma, M., Kurusu, M., Suzuki, K., Nishizono, A., Murakami, K., Fujioka, T. & Fujiki, H. (2005). New tumor necrosis factor-α-inducing protein released from *Helicobacter pylori* for gastric cancer progression. J. Cancer Res. Clin. Oncol. **131**, 305–313.

Suganuma, M., Kuzuhara, T., Yamaguchi, K. & Fujiki, H. (2006). Carcinogenic role of tumor necrosis factor-α inducing protein of *Helicobacter pylori* in human stomach. J. Biochem. Mol. Biol. **39**, 1–8.

Suganuma, M., Yamaguchi, K., Ono, Y., Matsumoto, H., Hayashi, T., Ogawa, T., Imai, K., Kuzuhara, T., Nishizono, A. & Fujiki, H. (2008). TNF-α-inducing protein, a carcinogenic factor secreted from *H. pylori*, enters gastric cancer cells. Int. J. Cancer, **123**, 117–122.

Szymczyna, B. R., Bowman, J., McCracken, S., Pineda-Lucena, A., Lu, Y., Cox, B., Lambermon, M., Graveley, B. R., Arrowsmith, C. H. & Blencowe, B. J. (2003). Structure and function of the PWI motif: a

novel nucleic acid-binding domain that facilitates pre-mRNA processing. Genes Dev. **17**, 461–475.

Terwilliger, T. C. & Berendzen, J. (1999). Automated MAD and MIR structure solution. Acta Crystallogr. sect. D Biol. Crystallogr. **55**, 849–861.

Terwilliger, T. C. (2003). Automated main-chain model building by template matching and iterative fragment extension. Acta Crystallogr. sect. D Biol. Crystallogr. **59**, 38–44.

Tosi, T., Cioci, G., Jouravleva, K., Dian, C. & Terradot, L. (2009). Structures of the tumor necrosis factor α inducing protein Tipα: A novel virulence factor from *Helicobacter pylori*. FEBS Lett. **583**, 1581–1585.

Yoshida, M., Wakatsuki, Y., Kobayashi, Y., Itoh, T., Murakami, K., Mizoguchi, A., Usui, T., Chiba, T. & Kita, T. (1999). Cloning and characterization of a novel membrane-associated antigenic protein of *Helicobacter pylori*. Infect. Immun. **67**, 286–293.

국문초록

Structural Basis for Differential Transcription Activation by Enantiomeric Agonists of PPARγ and Crystal Structure of TNF-α-Inducing Protein (Tipα) from *Helicobacter pylori*

PPARɣ 거울상 이성질체 작용제에 의한 차등 전사 활성화에 대한 구조 연구 및 헬리코박터 파이로리 유래 TNF-α-Inducing Protein (Tipα) 단백질에 대한 결정 구조 연구

퍼옥시좀 증식인자 활성화 수용체 감마 (PPARɣ)는 핵 수용체 슈퍼 패밀리의 구성원이다. 이것은 리간드에 의해 활성화되는 전사 인자로서 지방 세포 분화와 제 2 형 당뇨병 및 염증 조절의 중요한 역할을 감당한다. 수많은 PPARɣ 작용제는 알파나선 H12 근방의 표준 리간드 결합 주머니에 결합한다. 최근 연구를 통해서 PPARɣ 의 대체 리간드 결합 부위가 확인되었는데, 그것은 알파나선 H2'와 H3 사이의 오메가 루프 부근에 위치하고 있다. 본 연구의 선행 연구를 통하여 두개의 최적화 된 거울상 이성질체 PPARɣ 리간드 (S35 및 R35)의 분자 비대칭성이 PPARɣ 전사 활성과 결합력, Cdk5 매개 PPARɣ 273 번 세린 잔기 인산화 저해 활동도의 차이를 나타나게 함을 발표하였다. R35 는 기존 방식의 PPARɣ 작용제로 강력하게 작용하지만 S35 는 상당한 혈당 흡수 포텐셜을 가지는 PPARɣ 인산화 억제제로 작용한다. 이러한 리간드의 차등 활동에 대한 구조적 기초 제공을 위해 본 연구에서는 S35 와 R35 각각의 PPARɣ 리간드 결합 도메인 복합체의 결정 구조를 규명하였다. PPARɣ 리간드 결합 도메인 복합체의 구조는 이러한 거울상 이성질체 리간드의 결합 양식에서 상당한 차이를 드러냈다. R35 는 PPARɣ 작용제로서 표준 리간드 결합 주머니에 결합하는

반면 S35 는 대체 리간드 결합 부위를 차지하여, 두 이성질체의 서로 다른 행동 양식을 잘 설명한다. 이 연구 결과는 당뇨병 신약 후보로서 새로운 세대의 PPARɣ 리간드 개발에 유용한 환경을 제공할 것이다.

헬리코박터 파일로리균의 감염은 위암을 포함한 위·십이지장 질환의 가장 높은 위험 요인 중 하나이다. TNF-α 는 종양 촉진을 위해 필수적인 사이토카인 중의 하나이며, 따라서 TNF-α 의 발현을 유도하는 헬리코박터 파이로리균의 단백질은 인간의 위암 발생에 중요한 역할을 할 것으로 예상된다. 헬리코박터 파이로리 26695 균주의 HP0596 유전자 생성물은 TNF-α 유도 단백질 (Tipα)로 확인되었다. Tipα 는 이합체 상태로 헬리코박터 파이로리균에서 분비된 후, 위 세포로 침투한다. 이 단백질은 DNA 결합 활성을 갖는 것으로 나타났다. 본 연구에서는 헬리코박터 파이로리균 Tipα 단백질의 삼차원 구조를 규명하였다. Tipα 단백질의 단량체는 두 개의 구조적 도메인("혼합 도메인"과 "나선형 도메인")으로 구성되어 있다. Tipα 단백질은 결정 구조 내에서 이합체 상태로 존재하고, 이 이합체 구조는 DNA 결합을 위한 새로운 단백질 골격을 나타낸다. 알파나선 α1 과 α2 사이의 루프에 의해 Tipα 단백질 이합체의 두 단량체를 가로질러 형성된 양전하로 대전된 표면 부분이 DNA 결합에 중요 할 것으로 예측된다.

주요어: crystal structure / S35 / R35 / alternate ligand-binding site / Ω loop / peroxisome proliferator-activated receptor / type 2 diabetes / PPARγ agonist / tumor necrosis factor-α inducing protein / Tipα / HP0596 / *Helicobacter pylori* / gastric cancer